A New 1-hourly ERA5-based Atmosphere De-aliasing Product for GRACE, GRACE-FO, and Future Gravity Missions

Yang, Fan; Forootan, Ehsan; Wang, ChangQing ; Kusche, Jürgen; Luo, Zhi Cai

Published in:
Journal of Geophysical Research

DOI (link to publication from Publisher):
10.1029/2021JB021926

Publication date:
2021

Document Version
Accepted author manuscript, peer reviewed version

A New 1-hourly ERA5-based Atmosphere De-aliasing Product for GRACE, GRACE-FO, and Future Gravity Missions

Fan Yang[1,2], Ehsan Forootan[3], ChangQing Wang[4], Jürgen Kusche[5] and ZhiCai Luo[1,2]

[1]MOE Key Laboratory of Fundamental Physical Quantities Measurement and Hubei Key Laboratory of Gravitation and Quantum Physics,PGMF and School of Physics, Huazhong University of Science and Technology, Wuhan, P.R.China

[2]Institute of Geophysics and PGMF, Huazhong University of Science and Technology, Wuhan, P.R.China

[3]Geodesy and Earth Observation Group, Department of Planning, Aalborg University, Denmark

[4]Innovation Academy for Precision Measurement Science and Technology, Chinese Academy of Sciences, Wuhan, P.R.China

[5]Institute of Geodesy and Geoinformation, University of Bonn, Bonn, Germany

Key Points:

- Hourly ERA-5 reanalysis is employed to generate the atmosphere de-aliasing product for the first time, through a refined 3-D vertical integration method.
- The use of input fields from ERA-5 and increasing the sampling rate of atmospheric products to 1 hour are recommended for GRACE-FO and future missions.
- New sets of hourly atmospheric non-tidal de-aliasing and tidal components including $[S_1, S_2, P_1, K_1, N_2, M_2, L_2, T_2, R_2, T_3, R_3, S_3]$ are produced and freely shared.

Corresponding author: Ehsan Forootan, `efo@plan.aau.dk`

Abstract

The current state-of-the-art of satellite gravity data processing makes use of de-aliasing products to reduce high-frequency mass anomalies. For example, the most recent official Atmosphere and Ocean De-aliasing products (AOD1B-RL06) are applied for the Gravity Recovery and Climate Experiment (GRACE) and GRACE-Follow On (GRACE-FO) missions. The temporal resolution of AOD1B-RL06 is 3 hours, and spectrally, they are computed up to degree and order 180. In this study, we explore a refined, i.e., geometrically, physically, and numerically improved, mass integration approach that is important for computing the atmosphere part of these products. Besides, the newly available ERA-5 climate data are used to produce a new set of non-tidal atmosphere de-aliasing product (HUST-ERA5) that is computed hourly up to degree and order 100, covering 2002 onwards. Despite an overall agreement with AOD1B-RL06 (correlation$\geq$0.99), considerable discrepancies still exist between HUST-ERA5 and AOD1B-RL06. The possible reasons are therefore analyzed, and we find the input climate data, sampling rate and integration method may result in a product difference of $\sim$0.3, $\sim$0.15 and $\sim$0.05 millimeter geoid height, respectively. The total differences between HUST-ERA5 and AOD1B-RL06 can lead to a mean variation of $\sim$7.34 nm/s on the LRI (Laser Ranging Interferometry) range-rate residuals, for example during January 2019, which is already close to the LRI precision. This impact is invisible for the GRACE(-FO) gravity inversion because of the less accurate on-board KBR (K-band ranging) instrument, however, it will be non-negligible and should be considered when the LRI completely replaces the KBR in the future gravity missions.

Plain Language Summary

Time-variable GRACE and GRACE-FO satellite gravity data are unique remote sensing products that can be used for studying mass changes related to e.g., water variability in aquifers, continental ice-sheets, and oceans. The current state-of-the-art of GRACE(-FO) data processing makes use of background de-aliasing products to reduce high-frequency mass anomalies to focus on the dominant hydrology related signals. Thus, any errors in these products will badly affect the quality of water mass estimations. In this study, we explore a refined, i.e., geometrically, physically, and numerically improved, mass integration approach to use the newly available ERA-5 weather data for computing the atmosphere part of the background non-tidal de-aliasing products. The new set is called HUST-ERA5 that is computed hourly up to degree and order 100, covering 2002 onwards, and freely available for download. Here we show that replacing the official de-aliasing products with HUST-ERA5 can lead to a mean variation of 7.34 nm/s on the Laser Ranging Interferometry (LRI) residuals, which is close to the LRI precision. This impact is invisible for the GRACE(-FO) data because of the less accurate on-board ranging instrument. However, it will be non-negligible and should be considered when the LRI is functional in the future gravity missions.

1 Introduction

The Gravity Recovery and Climate Experiment (GRACE, 2002-2017) mission (Tapley et al., 2004), together with its successor GRACE follow-on (2018-onwards) mission (Kornfeld et al., 2019), have collected numerous valuable observations that allow mapping the Earth's time-variable gravity field. Applications that utilize these fields (e.g., Dahle et al., 2014) have broadened our knowledge in interdisciplinary science including studying water variability in aquifers (Ramillien et al., 2011; Famiglietti & Rodell, 2013; Schumacher et al., 2018; Mehrnegar et al., 2021), continental ice-sheets (Sasgen et al., 2013; Velicogna et al., 2020), and geo-dynamics (Panet et al., 2018) at meso-scale, i.e., 10 to few 100 kilometers (see other examples in, e.g., Kusche et al., 2012; Tapley et al., 2019).

Other candidate gravity missions as a successor of GRACE-FO, such as those of the Next-Generation Gravity Mission (NGGM), are also under investigation (Pail et al., 2018). However, the temporal aliasing due to the poor sampling of high frequency ocean and atmospheric mass variations represents a dominant error source (Behzadpour et al., 2019) even for a substantially improved instrument such as the LRI (Laser Ranging Interferometer), so that the usage of more precise sensors cannot meet its full potential (Flechtner et al., 2016; Yang et al., 2018; Cambiotti et al., 2020). This may also happen to the NGGM unless the state-of-the-art of processing is revised (Daras & Pail, 2017; Hauk & Pail, 2018).

At present, the non-tidal part of the high frequency mass variations is modeled by applying the background Atmosphere and Ocean De-aliasing products (known as AOD1B) maintained by the GeoForschungsZentrum (GFZ) Potsdam (Dobslaw et al., 2017b). These products contain the ocean and atmosphere parts, and this paper focuses on the computation of the atmospheric part of AOD1B, in which multi-level atmosphere fields are converted to potential coefficients and their contribution is removed from in-orbit gravity gradients. This conversion has been realized using i.e., a three-dimensional (3-D) integration approach including various approximations (see e.g., Boy & Chao, 2005; Forootan et al., 2013; Flechtner et al., 2014). Many efforts have been made by previous studies to improve the atmospheric de-aliasing modelling, for example, increasing the spatial and temporal resolution of its input fields, improving its long-term consistency, and considering a realistic parameterization for solving its 3-D mass integral (e.g., Forootan et al., 2013; Hardy et al., 2017).

Seen from the AOD1B history, great attempts have been made by GFZ to improve the quality. For instance, the ECMWF (European Centre for Medium-Range Weather Forecasts)'s ERA40 ($\sim$110 km, 6 hours, 60 layers), ERA-interim ($\sim$79 km, 6 hours, 60 layers), as well as operational atmosphere fields ECMWF (2015a, 2015b) were tested as inputs of AOD1B, where each showed their advantages and limitations (Dobslaw et al., 2017a). The latest release of AOD1B (RL06) successfully combines the short-term (3 hourly and even hourly) forecasts and 6-hour operational data to provide the atmospheric de-aliasing product at 3 hourly resolution and up to degree and order 180 (Dobslaw & Thomas, 2005). Nevertheless, the forecast climate data is less reliable, and the operational data is temporally less consistent than the reanalysis (ERA40 and ERA-interim). Therefore, a further improvement in the AOD modeling can be expected by replacing the input climate data with a higher spatial, temporal, and vertical resolution, as well as with a better long-term consistency to prevent temporal biases (see Forootan et al., 2014). Here, we test the newly published long-term (1979 onwards) multi-level reanalysis from ECMWF (ERA-5, Hersbach et al., 2020) with unprecedented spatial, temporal, and vertical resolution: $\sim$35 km, 1-hour, and 137 layers. We expect that using these fields may offer a better resource to compute non-tidal atmosphere de-aliasing products that are of higher quality than the atmospheric part of RL06.

In addition to the input climate data, there is also room to improve the numerical integration method. Swenson and Wahr (2002) indicated the vertical structure of the atmosphere must be considered for producing the AOD products. Boy and Chao (2005) suggested a 3D integration that considers surface pressure fields, as well as its upper layers, which was though simplified in the subsequent AOD modeling (Flechtner et al., 2014). Unlike the previous attempts, the latest AOD1B RL06 divides the atmosphere into two parts (surface pressure and upper air anomaly), rather than regarding them as a whole as was done in previous products. Thanks to this separation, each compartment can be more precisely modeled with individual and special treatment (Dobslaw et al., 2017b). In this study, we proposes an estimation of the atmospheric mass by combining the suggested 'separation' of RL06 and possible physical, geometrical, and numerical modifications (by modifying the ITG-3D formulation in Forootan et al., 2013).

Using the modified 3D integration method and the multi-level ERA-5 reanalysis data as input, a new set of atmospheric de-aliasing product called HUST-ERA5 is produced that covers 2002 onwards (covering the lifetime of GRACE and GRACE-FO). The new product has the temporal sampling rate of 1 hour that is computed in terms of spherical harmonics up to degree and order 100 ($\sim$200 km spatial resolution). HUST-ERA5 is publicly available online via `https://data.tpdc.ac.cn/en/data/52201272-bf8d-41bd-aff6-020dd1caeeda/`, see also Yang and Luo (2021). Assessments on HUST-ERA5 are also made with the official AOD-RL06 products to demonstrate the impact of ERA-5 data as well as the proposed method. In particular, the LRI range-rate measurements acquired by GRACE-FO are analyzed to quantify the impact sensed at the orbital level. We explain that LRI has a higher sensitivity than KBR (K-band ranging, i.e., previously used in Yang et al., 2018, for validating GRACE data). Therefore, they can be used as a reliable measure to uniquely detect un/mismodeled shortwavelength gravitational perturbations as shown by Ghobadi-Far et al. (2020). Moreover, future gravity missions will likely carry LRI instrument, which makes it possible to assess HUST-ERA5 for future applications.

In what follows, in Sec. 2, a brief introduction of atmosphere input data as well as the GRACE(-FO) L1b data is provided. In Sec. 3, the methodology of atmospheric tidal and non-tidal modeling is explained, and the proposed refined mass integral method of this study is introduced. In Sec. 4, the obtained tidal constitutions such as S_1 and S_2 are firstly compared to those of RL06, and subsequently, HUST-ERA5 and RL06 non-tidal products are assessed in details. Sec. 5 concludes the paper and provides possible extensions of this study.

2 Data

2.1 Atmosphere input data

ERA-5 is the latest ECMWF (European Centre for Medium-Range Weather Forecasts) reanalysis, which provides hourly estimates of atmospheric variables globally with the spatial resolution of $\sim$31 km and the vertical resolution of 137 hybrid sigma/pressure (model) levels from the surface of Earth up to the height of 80 km (top level at 0.01 hPa). ERA-5 combines vast amounts of historical observations into global estimates using 4D-Var data assimilation in CY41R2 of ECMWFs Integrated Forecast System (IFS), thus, it can be assumed as the most precise representation of the state of atmosphere among the current ECMWF product series. More information on ERA-5 can be found in its technical document (`https://confluence.ecmwf.int/display/CKB/ERA5\%3A+data+documentation`). The input atmosphere fields of ERA-5 are downloaded from `http://climate.copernicus.eu/climate-reanalysis`. ERA-interim is the recently retired ECMWF's reanalysis that covers the period of 1989-2019. This data is generated by the IFS CY31R2 with the spectral T255 model ($\sim$79 km globally) in the horizontal, with 60 vertical model levels, and with the temporal resolution of every 6 hours. More information can be found in Dee et al. (2011) and Berrisford et al. (2011). These fields are downloaded from `http://www.ecmwf.int/en/research/climate-reanalysis/era-interim`. The ERA-5 and ERA-interim atmospheric fields can be applied for producing de-aliasing data that are used for comparisons of this study. HUST-ERA5 is computed using ERA-5, and the results are compared to the atmospheric part of GFZ AOD1B-RL06 (Dobslaw et al., 2017a).

2.2 GRACE(-FO) L1b data

A set of GRACE(-FO) L1b data is used to compute range-rate residuals for assessments (Wen et al., 2019). The dataset we used contains the K-band microwave ranging rate (KBRR), Laser Ranging Interferometry (LRI) range rate, GPS positions, 3-axis accelerometer measurements along with the star camera measurements (Vielberg et al., 2018) and AOD1B. All the data, mentioned above, are accessible at `ftp://isdcftp.gfz-potsdam.de`. In addition, the kinematic orbit form TU Graz is employed as an alternative orbit option (`ftp://ftp.tugraz.at/outgoing/ITSG/tvgogo/orbits/`). Our study will utilize the L1b data in our in-house gravity recovery software HAWK, and LRI range-rate residual is used to evaluate the results as Dobslaw et al. (2017b); Yang et al. (2018).

3 Methodology

The computation of HUST-ERA5 is based on a complete implementation of the atmospheric part of RL06's method with an extension of (physical, geometrical and numerical) modifications raised by Forootan et al. (2013). The overall flowchart of the data processing of this study is presented in Figure 1, where the most critical steps would be individually explained in the following.

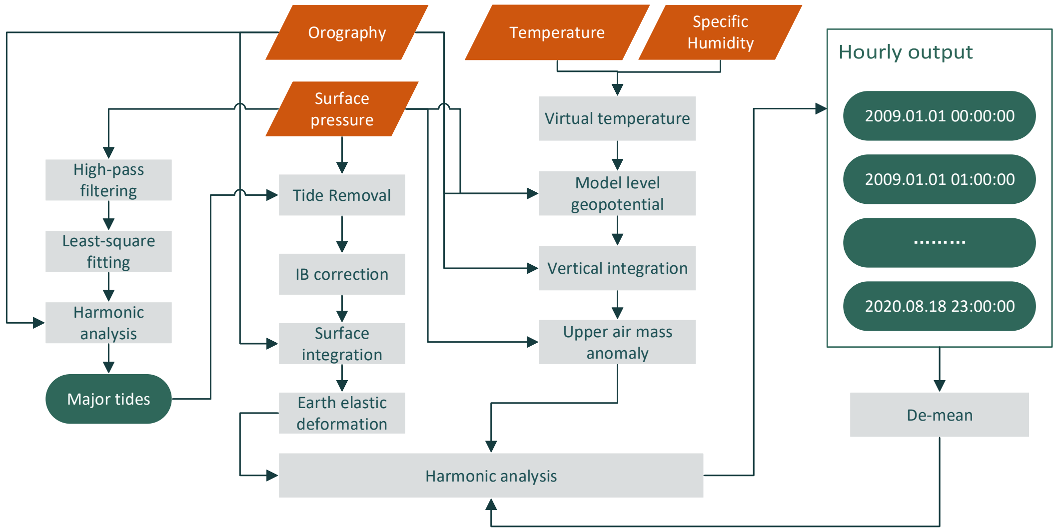

Figure 1. The computation steps of HUST-ERA5 atmospheric de-aliasing products. The inputs are highlighted in orange and the outputs are filled by the dark green color.

3.1 Removing the dominant tidal frequencies

By definition, the AOD products must not contain tidal oscillations. However, the input pressure fields contain a mixture of tidal and non-tidal constitutes, which need to be separated. The attributions of generally used atmospheric tides are presented in Table 1, where the solar tides S_1 (diurnal tide) and S_2 (semi-diurnal tide) are the principal ones (i.e., their magnitudes are considerably larger than the others $[P_1, K_1, N_2, M_2, L_2, T_2, R_2, T_3, R_3, S_3]$). Previous studies showed that the tidal constitutions can be well fitted and represented from the ERA-interim surface pressure fields (i.e. Biancale & Bode, 2006), though their amplitudes were slightly different from the ones derived from observations (Schindelegger & Ray, 2014).

We therefore extend the experience by Dobslaw et al. (2017b) to consider the ERA-5 dataset for extracting the contribution of S_1 and S_2 frequencies as well as the other ten small tides from these fields covering 2002 onwards. With the tide information in Table 1, the Earth surface pressure caused by tides can be regarded as a summation of the frequency-dependent tidal pressure ζ_s with the amplitude ξ_s and phase δ_s for a given tide s at an arbitrary point (θ, λ) and a distinct time t (Petit & Luzum, 2010) as

$$\zeta(\theta, \lambda, t) = \sum_s \xi_s(\theta, \lambda) \cos[\omega_s t + \chi_s - \delta_s(\theta, \lambda)], \tag{1}$$

Table 1. Tidal constitutes estimated and removed from surface pressures following the recommendations of AOD1B RL06 (Dobslaw et al., 2017b).

Name	Doodson No.	deg/hr (ω)
P_1	163.555	14.9589314
S_1	164.556	15.0000000
K_1	165.555	15.0410686
N_2	245.655	28.4397295
M_2	255.555	28.9841042
L_2	265.455	29.5284789
T_2	272.556	29.9589333
S_2	273.555	30.0000000
R_2	274.554	30.0410667
T_3	381.555	44.9589300
S_3	382.555	45.0000000
R_3	383.555	45.0410700

where ω_s denotes the frequency of tides to be estimated (see Table 1), χ_s is the Warburg phase correction as shown in Petit and Luzum (2010), (θ, λ) denotes the spherical coordinate (colatitude, longitude). Equation (1) can also be rewritten as

$$\begin{aligned} \zeta(\theta, \lambda, t) &= \sum_s [\xi_s \cos(\chi_s - \delta_s)\cos(\omega_s t) + \xi_s \sin(\delta_s - \chi_s)\sin(\omega_s t)] \\ &= \sum_s [A_s(\theta, \lambda) cos(\omega_s t) + B_s(\theta, \lambda) sin(\omega_s t)], \end{aligned} \tag{2}$$

where $\xi_s \cos(\chi_s - \delta_s)$ and $\xi_s \sin(\delta_s - \chi_s)$ are relabelled as $A_s(\theta, \lambda)$ and $B_s(\theta, \lambda)$. In this manner, the ERA-5 surface pressure time-series $P(\theta, \lambda, t)$ can be factorized into the following constitutions, i.e, the tidal part $\zeta(\theta, \lambda, t)$ and the non-tidal part as

$$P(\theta, \lambda, t) \quad = \textstyle\sum_s [A_s(\theta, \lambda) cos(\omega_s t) + B_s(\theta, \lambda) sin(\omega_s t)] + C(\theta, \lambda)t + D(\theta, \lambda) + e, \tag{3}$$

where terms of trend $C(\theta, \lambda)$ and bias $D(\theta, \lambda)$ are considered, and the residual e is assumed as the white noise to enable a Least Squares (LS) fit. The terms $A_s(\theta, \lambda)$ and $B_s(\theta, \lambda)$ contain the information about tidal amplitude and phase. However, before the LS fitting, a high-pass filtering is applied to remove low-frequency 'noise components' that are slower than those of tides. For this, a 3rd-order Butterworth filter (Butterworth, 1930) associated with a cutoff frequency of 3 days is applied as in Dobslaw et al. (2017b). The design of the n'th-order Butterworth low-pass filter follows

$$H(j\omega) = \frac{1}{\sqrt{1 + \epsilon^2 (\frac{\omega}{\omega_C})^{2n}}}, \tag{4}$$

where n is the order of the filter ($n = 3$ in this study), ω is the operating frequency (pass-band frequency) of circuit, ω_C is the cutoff frequency ($\omega_C = 3 \times 24$ hours $= 3$ days in this study), and ϵ is the maximum pass band gain.

Figure 2 demonstrates the impact of the band-pass filter in Eq. (4) and the LS fit of Eq. (3) for a point with latitude 0° and longitude W180° (randomly selected) over the period of 2009-2012. It can be seen from Figure 2 that there is a peak that corresponds to frequency ~ 0 hour, as well as two dominant peaks related to the S_1 and S_2 frequencies, see Figure 2(a-b). However, the effect of low-frequencies is well damped after implementing the high-pass filter, see Figure 2(c-d). By implementing the LS fit, the contribution of S_1 and S_2 frequencies is considerably reduced as well, i.e., one can expect $\sim 80\%$ reduction in the magnitude of these frequencies, see Figure 2(e-f). Here, Figure 2 considers only S_1 and S_2 frequencies as an example, while all the 12 tides in Table 1 are reduced before producing HUST-ERA5.

The approach presented in Figure 2 can be followed to estimate the point-wise $A_s(\lambda, \theta)$ and $B_s(\lambda, \theta)$ for a given tidal frequency. By substituting these parameters back into Eq. (2), tidal contribution $\zeta_s(\theta, \lambda, t)$ of that frequency can be calculated and removed from the original surface pressure time-series as

$$\begin{aligned} R(\theta, \lambda, t) &= P(\theta, \lambda, t) - \zeta(\theta, \lambda, t) = P(\theta, \lambda, t) - \sum_s \zeta_s(\theta, \lambda, t) \\ &= P(\theta, \lambda, t) - \sum_s [A_s(\theta, \lambda) cos(\omega_s t) + B_s(\theta, \lambda) sin(\omega_s t)], \end{aligned} \tag{5}$$

where $R(\theta, \lambda, t)$ is the residuals that expect to be converted into the atmospheric de-aliasing product later on. Subsequently, the potential coefficients [cnmCos, snmCos] and [cnmSin, snmSin] up to degree/order 180 are respectively transformed from $0.5° \times 0.5°$ gridded $A_s(\theta, \lambda)$ and $B_s(\theta, \lambda)$, through the surface integration technique (see Section 3.3) and the harmonic analysis method (see Section 3.6). The potential coefficients of each tide are provided at a data repository site (Yang, 2021), following the standard gravity field format. Having the potential coefficients, a specific atmosphere tide $\zeta_s(\theta, \lambda, t)$ at an given epoch t can be readily

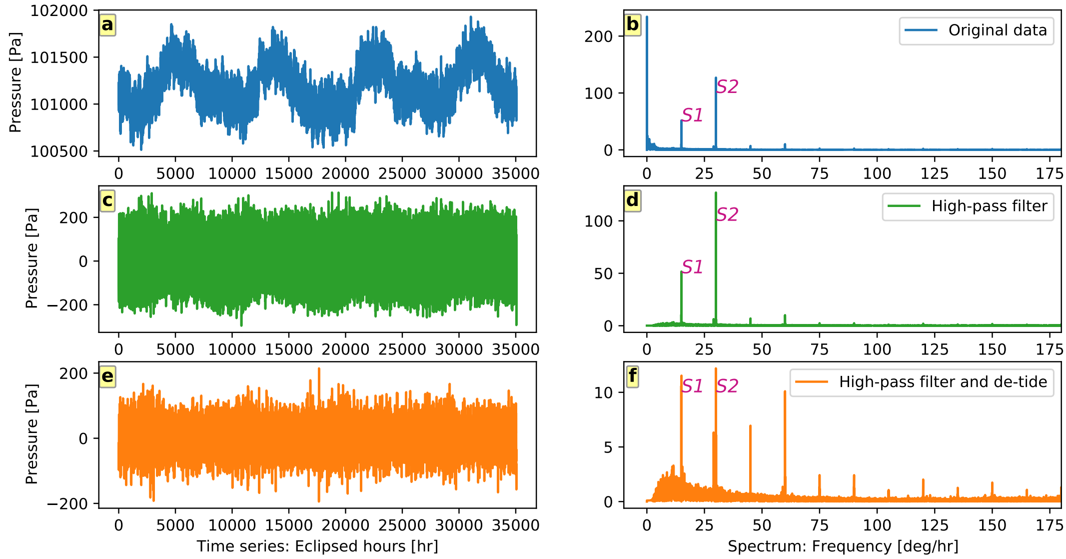

Figure 2. A demonstration of the reduction of tidal frequencies at a point with latitude 0° and longitude W180° during the period of 2009-2012. In the figure, (a) is the original surface pressure time-series from ERA-5, and meanwhile its frequency spectrum after removing the mean is given in (b). (c) denotes the time-series after applying the Butterworth high-pass filter to (a), and its frequency spectrum is shown in (d). The last row (e-f) represents the results after reducing S_1 and S_2 frequencies from (c) and (d).

retrieved as

$$\begin{aligned} C_{nm}^{s} &= cnmCos\cos(\omega_s t) + cnmSin\sin(\omega_s t) \\ S_{nm}^{s} &= snmCos\cos(\omega_s t) + snmSin\sin(\omega_s t), \end{aligned} \tag{6}$$

where the derived $[C_{nm}^s, S_{nm}^s]$ is the spherical harmonic expansion of tide $\zeta_s(\theta, \lambda, t)$ at a specified degree n and order m. Note that the Doodson-Warburg phase corrections χ_s in Eq. (1) are already applied to the provided coefficients and therefore do not have to be considered once again, see also in Rieser et al. (2012).

3.2 IB correction

Although the surface pressure over the oceans is unevenly distributed, the local sea surface normally reacts rapidly with the air pressure variations and adjusts itself perfectly to reach a balance with the air pressure. To remain the overall static contribution of atmosphere over the oceans, the Inverted Barometer (IB) correction is applied (Dobslaw et al., 2017a). Practically, to implement the IB correction, one should replace the pressure p_s at every grid point over the oceans with the area-mean surface pressure $\hat{p}_s$ averaged over the whole ocean domain as defined by the land-sea mask $S(\theta, \lambda)$, while keeping the pressure over the continents unchanged. This is done as

$$\hat{p}_s = \frac{1}{A_{ocean}} \iint p_s dA, \tag{7}$$

where A denotes the area. To acquire the corrected pressure $\hat{p}_s$, we implement a latitude-dependent weighting function in the grid domain as

$$\hat{p}_s(\theta, \lambda) = \frac{\sum_{-\pi/2}^{\pi/2} \sum_0^{2\pi} S(\theta, \lambda) p_s(\theta, \lambda) \cos(\theta)}{\sum_{-\pi/2}^{\pi/2} \sum_0^{2\pi} S(\theta, \lambda) \cos(\theta)}, \tag{8}$$

where (θ, λ) represents the spherical coordinates as Eq. (1). It is apparent that the definition of the land-sea mask $S(\theta, \lambda)$ makes a difference on the final result. Therefore, we publicly share the land-sea mask used in this study for check (Yang, 2021), which is expanded in terms of spherical harmonic up to degree and order 360. It should be noticed that the IB-correction is applied to the residual pressure fields after removing the contribution of tides as described in Eq. (5). It is also worth mentioning, Ponte (1993) points out that IB-correction is not reliable for periods shorter than approximately 2 days, indicating that considering a correction over a longer period rather than 1-hour in this study is necessary. Nevertheless, we still make the correction per hour to be consistent with the official AOD product.

3.3 Surface integral

Newton's law allows for a unique gravity field determination from an integration of arbitrary mass distribution on or above the Earth (see, e.g., Chao, 2005) using the same notation in Swenson and Wahr (2002) as

$$\Delta C_{nm} + i\Delta S_{nm} = \frac{3}{4\pi\rho_e} \frac{1+k_n}{2n+1} \int_0^{2\pi} \int_0^{\pi} \Delta I_n(r, \theta, \lambda) P_{nm}(\cos\theta) e^{im\lambda} \sin\theta d\theta d\lambda, \tag{9}$$

where (r, θ, λ) are spherical coordinates of a given point (radial distance, colatitude, and longitude) in the terrestrial reference frame; $P_{nm}(\cos\theta)e^{im\lambda}$ as a whole represents the 4π-normalized surface spherical harmonics; k_n is the loading love number, inferring that an indirect effect caused by Earth deformation has been considered already; ρ_e is the Earth mean density; $[\Delta C_{nm}, \Delta S_{nm}]$ is the gravity spherical harmonic coefficients at degree n and order m; ΔI_n is the so-called degree-dependant inner integral that has a critical contribution on the computation of AOD products (Forootan et al., 2013). In general, ΔI_n is calculated by integrating all the known mass over the Earth as

$$\Delta I_n(r,\theta,\lambda) = \int_0^{+\infty} (\frac{r}{a_e})^{n+2} \rho(r,\theta,\lambda) dr \tag{10}$$

where a_e is the Earth's mean radius, which is often chosen as the semi-major axis (6378136.6 km) of the reference ellipsoid; $\rho(r,\theta,\lambda)$ is the point-wise mass density; r represents actually the distance of test mass from the Earth center, see Figure 3, which consists of the ellipsoidal radius a, the geoid undulation h, the orography ζ, and the geometric height z of the point above the orography as

$$r(\theta,\lambda) = a(\theta,\lambda) + \zeta(\theta,\lambda) + h(\theta,\lambda) + z(\theta,\lambda). \tag{11}$$

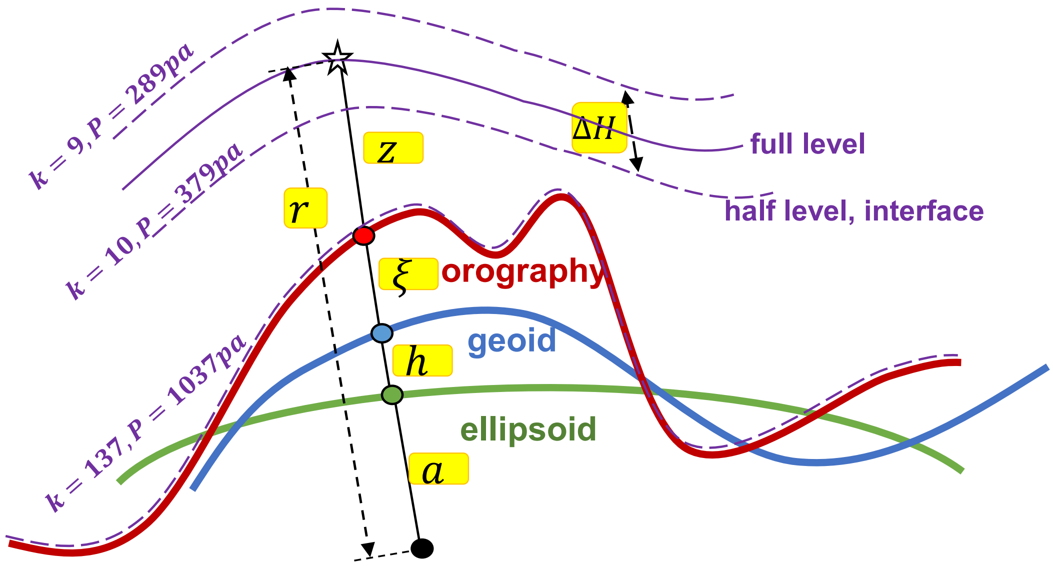

Figure 3. An overview of the Earth's surface geometry and its relationship with atmospheric model levels. The components $[a, h, \zeta, z]$ constitute the distance r from an exemplary point shaped by a star to the Earth's center of mass. The definition of $[a, h, \zeta, z]$ refers to Eq. (11). The model's vertical levels (from the topmost $k = 1$ to the bottom $k = 137$ level) are shown by the solid purple lines and the half-levels are shown by the purple dashed lines.

Once the mass anomaly is expected to occur only at a thin layer on the Earth's surface, the computation of ΔI_n in Eq. (10) can be facilitated by a simple 'surface integral'; Otherwise, such a process has to be done by a complex 'vertical integral'. This section mainly deals with the first case, where the atmosphere mass from its top (pressure ∼0 pa) to the Earth's surface (see the red curve of Figure 3) are all assumed to be compressed into the

Earth's surface. By this assumption, ΔI_n can be simplified as

$$\Delta I_n(r, \theta, \lambda) = (\frac{a(\theta, \lambda) + \zeta(\theta, \lambda) + h(\theta, \lambda)}{a_e})^{n+2} \frac{\Delta P_0(r, \theta, \lambda)}{g(r, \theta, \lambda)}, \tag{12}$$

where $g(\theta, \lambda, r)$ represents the point-wise gravity acceleration; ΔP_0 indicates the surface pressure. The detailed deduction of Eq. (12) can be found in Boy and Chao (2005). The parameters involved in the computation of the inner integral are listed in Table 2.

Table 2. A summary of the variables/parameters/constants for the calculation of the inner integral ΔI_n in this study.

Constant	Value	Description	Source and Ref.
a_e	6378136.6 m	Equatorial radius of the Earth	IERS2010[a] (Petit & Luzum, 2010)
ρ_e	5517 kg/m^3	Earth mean density	Wahr et al. (1998)
g_{wmo}	9.80665 m/s^2	Mean gravity	Defined by WMO[b]
R_{dry}	287 $J/Kg \cdot K$	Dry air constant	ECMWF (2015b)
R_{vap}	174 $J/Kg \cdot K$	Water vapor constant	ECMWF (2015b)
k_n	dimensionless	Load Love number	Wang et al. (2012)
$a(\theta, \lambda)$	m	Ellipsoidal radius of the Earth	GRS80 (Petit & Luzum, 2010)
$\zeta(\theta, \lambda)$	m	Geoid undulation	XGM2019e (Zingerle et al., 2020)
$h(\theta, \lambda)$	m	Topography/Orography	ERA-5 (Hersbach et al., 2020)
$z(\theta, \lambda)$	m	Orthometric height	ERA-5 (Hersbach et al., 2020)
$g(r, \theta, \lambda)$	m/s^2	Gravity acceleration	XGM2019eZingerle et al. (2020)

[a] is the abbreviation of International Earth Rotation and Reference Systems Service.

[b] is the abbreviation of World Meteorological Organization.

3.4 Vertical integral

Swenson and Wahr (2002) indicated that applying only a surface integration would introduce errors into the GRACE time-variable surface mass signal, up to a few millimeters equivalent water thickness, therefore the vertical integration that enables a consideration of the vertical profile of the atmosphere is recommended. In such a case, multi-levels atmosphere input fields are required, i.e., ERA-interim with max layer $k_{max} = 60$, or ERA-5 with $k_{max} = 137$. These layers are defined in a convention of sigma model-level, see ECMWF (2015a). Another important concept, the 'half-level' represents actually the interfaces between these layers, see Figure 3. A typical example of the 'half-level is the surface orography, which corresponds to $k = k_{max} + 1/2$ as the lower boundary of the atmospheric column. On the contrary, the topmost layer with the pressure value of ~ 10 Pa corresponds to $k = 1$, as a matter of convention.

Substituting Eq. (11) into Eq. (10) provides the 3D vertical integral formulation as

$$\Delta I_n(r, \theta, \lambda) = \int_0^{+\infty} (\frac{a(\theta, \lambda) + \zeta(\theta, \lambda) + h(\theta, \lambda) + z(\theta, \lambda)}{a_e})^{n+2} \frac{dp(r, \theta, \lambda)}{g(r, \theta, \lambda)}, \tag{13}$$

which can be written in a discrete format by leveraging the multi-level climate fields as

$$\Delta I_n(r, \theta, \lambda) = \sum_{k=0}^{k_{max}} (\frac{a(\theta, \lambda) + \zeta(\theta, \lambda) + h(\theta, \lambda) + z_k(\theta, \lambda)}{a_e})^{n+2} \frac{\Delta P_k(\theta, \lambda, r_k)}{g_k(\theta, \lambda, r_k)}. \tag{14}$$

In this equation, for each level k, $\Delta P_k(\theta, \lambda, r, t)$ denotes the pressure difference between $[k + 1/2]$ interface and the next interface $[k - 1/2]$. The pressure at a given interface, i.e., $[k + 1/2]$, can be uniquely determined with the surface pressure P_0 and the level-dependent coefficients $[a_k, b_k]$ by

$$\begin{aligned} P_{k+1/2} &= a_{k+1/2} + b_{k+1/2} P_0, \\ \Delta P_k &= P_{k+1/2} - P_{k-1/2} = a_{k+1/2} - a_{k-1/2} + (b_{k+1/2} - b_{k-1/2}) P_0, \end{aligned} \tag{15}$$

where the surface pressure P_0 along with the coefficients $[a_k, b_k]$ are publicly available from the reanalysis data. So that, only $[a, \zeta, h, z_k]$ remains to be estimated for calculating ΔI_n in Eq. (13), where the previous three parameters $[a, \zeta, h]$ are straightforward and simple since they are level-independent, see Table 2. On the contrary, computing z_k (the geometric height of k'th layer above the orography) is complicate, since this requires calculating the geopotential H_k and translating it to the geometric height z_k. The translation method has been intensively addressed and we won't repeat again, please refer to Boy and Chao (2005). Thus we only need to calculate the geopotential height at k'th layer, which can leverage a recursive calculation of the differences ΔH (see Figure 3) for adjacent levels, i.e.,

$$\Delta H = H_{k+1/2} - H_{k-1/2} = -\frac{R_{dry} T_v^k}{g_{wmo}} \ln \frac{P_{k+1/2}}{P_{k-1/2}}. \tag{16}$$

In this way, the geopotential height differences ΔH can be subsequently integrated vertically upwards to obtain the $H_{k+1/2}$ by starting from the Earth's surface as

$$H_{k+1/2} = H_s + \sum_{j=k+1}^{k_{max}} \frac{T_v^j R_{dry}}{g_{wmo}} \ln \frac{P_{j+1/2}}{P_{j-1/2}}, \tag{17}$$

with

$$T_v^j = T^j [1 + \{R_{vap}/R_{dry} - 1\} q^j], \tag{18}$$

where g_{wmo} is the constant gravity acceleration and (R_{vap}, R_{dry}) denote the gas constants for water vapor and dry air, respectively. These constants are predefined in Table 2. Besides, (T_v^j, T^j, q^j) represent the virtual temperature, the temperature, and the specific humidity at j'th layer. Among these variables, the orography H_s as well as the level-dependent $[T^j, q^j]$ are all available from the reanalysis dataset. It is worth mentioning that, the aforementioned computation procedures are all defined at full model levels (i.e., ΔP_k) rather than half levels, see the star-shaped point in Figure 3(a). Nevertheless, one can easily switch the vertical integral to the half level $\Delta P_{k+1/2}$ by applying a simple linear interpolation.

3.5 Refined vertical integral

As of now, it can be seen from Eq. (11) and Eq. (14) that, the vertical integration ΔI_n is heavily dependent on the variables $[r, \Delta P, g]$. Therefore, any refinement on these variables will facilitate a more precise estimation of ΔI_n. As a reference, the vertical integration, in terms of $[r, \Delta P, g]$ that follows the definition of RL06, is called the 'normal' vertical integral (abbreviated as NVI). On the contrary, we demonstrate some possible refinement in the geometrical, physical and numerical aspects of these variables $[r, \Delta P, g]$, based on the approach suggested in Forootan et al. (2013). This refined method is abbreviated as 'RVI' hereinafter.

For RVI, firstly, the distance r in Eq. (11) is refined by adding the component of geoid undulation h that was neglected in RL06. Calculating the geoid undulation needs a static gravity model along with a reference ellipsoid. In this study, GRS80 is chosen as the reference ellipsoid, and meanwhile the latest static gravity model XGM2019e up to degree and order 5399 that corresponds to a spatial resolution of $\sim$4 km is employed (Zingerle et al., 2020).

Having all prepared, the geoid undulation h is derived from

$$h(\theta, \lambda) = a_e \sum_n \sum_m P_{nm}(\cos\theta)[C_{nm}\cos m\lambda + S_{nm}\sin m\lambda], \tag{19}$$

where all the variables follows the same definition described in the previous section.

Secondly, unlike the previous studies that used a latitude-dependent formulation to compute the gravity acceleration (i.e., Swenson & Wahr, 2002; Boy & Chao, 2005; Forootan et al., 2013), we evaluate $g(r, \theta, \lambda)$ with an exact method that completely considers the latitude, the altitude as well as the longitude by computing the first order derivative of the gravity potential (see Barthelmes, 2013). Mathematically, the $g(r, \theta, \lambda)$ by request can be always related to the $g^*(\theta, \lambda)$ on the Earth surface by an upward continuation as

$$g(r, \theta, \lambda) = (\frac{a_e}{r})^2 g^*(\theta, \lambda), \tag{20}$$

where the surface gravity accelerations g^* can be calculated with the first order derivative of XGM2019e (Zingerle et al., 2020) as mentioned before. In this means, one can compute an accurate gravity acceleration for an arbitrary point above the Earth with Eq. (20).

At last, wo propose to densify the vertical resolution of the atmospheric fields in Eq. (13) as it may influence the approximation of the inner integral ΔI_n. For example, we use the ERA-5 fields, which compared to its previous version ERA-interim, are better vertically resolved, i.e., the number of ERA-5's vertical levels is 137, while that of ERA-interim was 61. We also find that, the vertical profile of temperature and humidity follows a smooth and slow level-to-level change, which enables a linear interpolation of these variables to further densify the vertical layers of ERA-5. In this way, we derive an additional set of temperature and humidity at the middle of layer k and layer $k+1$, i.e.,

$$\begin{cases} T_{new} = \frac{1}{2}(T_k - T_{k+1}) \\ q_{new} = \frac{1}{2}(q_k - q_{k+1}) \\ P_{new} = \frac{1}{2}(P_k - P_{k+1}) \\ T_v^{new} = T_{new}[1 + \{R_{vap}/R_{dry} - 1\}q_{new}] \\ H_{new} = H_{k+1/2} + \frac{R_{dry}T_v^{new}}{g_{wmo}} \ln \frac{P_{k+1/2}}{P_{new}}. \end{cases} \tag{21}$$

The newly added layer outlined above is different with that of Forootan et al. (2013), where they implemented a direct interpolation of ΔI_n rather than an interpolation of physical variables that is suggested in this study. A direct interpolation might be less precise because the term ΔI_n in Eq. (14) is not a simple linear combination of the physical variables. On the contrary, the non-linear behaviors of the vertical profiles are well retained in our method, but they are densified. It is worth mentioning that this interpolation does not add any physical information, nevertheless the bonus comes from the numerical aspect since the better resolution improves estimating the vertical integral.

3.6 A combination of surface integral and vertical integral

As discussed in Dobslaw et al. (2017a), the atmospheric gravitational effect comes from two contributions: one is the surface pressure, and another is the upper air mass anomaly. These two contributions are basically different, for instance, both surface pressure and upper air cause a direct gravitational effect, whereas only surface pressure leads to another indirect effect due to Earth deformation as much as the load love numbers allow. Besides, IB-correction (see Eq. (8)) is only applied to the surface pressure rather than the upper air mass anomaly. As well, tidal removal is found considerable for the surface pressure, whereas it is unnecessary for the upper air mass anomaly (Dobslaw et al., 2017a). Therefore, a separation of surface pressure and upper air mass anomaly is required, so that aforementioned treatments such as IB correction and tidal removal can be made individually. Such a separation is realized by combining the surface integral and vertical integral, i.e., the surface $\Delta I_n^{surface}$ and upper air $\Delta U_n = \Delta I_n^{vertical} - \Delta I_n^{surface}$ components.

As Eq. (9) has already considered the indirect gravitational effect, the final inner integral of our product HUST-ERA5 is expressed as:

$$\Delta I_n = (\Delta I_n^{surface} - I_n^{tide} + I_n^{IB}) + \frac{1}{1+k_n}(\Delta I_n^{vertical} - \Delta I_n^{surface}), \tag{22}$$

where the term in the first bracket denotes the contribution from surface pressure after tide-correction I_n^{tide} and IB-correction I_n^{IB}; the term in the second bracket denotes the contribution from the upper air mass anomaly after removing the indirect gravitational effect by dividing $1 + k_n$. At last, as the time-mean makes no sense for temporal gravity field inversion from GRACE, we remove the mean of ΔI_n from Eq. (9) following the way of the official AOD products, which gives

$$\Delta C_{nm} + i\Delta S_{nm} = \frac{3}{4\pi\rho_e}\frac{1+k_n}{2n+1}\int_0^{2\pi}\int_0^{\pi}(\Delta I_n - \Delta\bar{I}_n)P_{nm}(\cos\theta)e^{im\lambda}\sin\theta d\theta d\lambda, \tag{23}$$

where $\Delta\bar{I}_n$ denotes the mean of ΔI_n over the years 2007-2014. Following Sneeuw (1994), a two-step method is applied to numerically solve Eq. (23) as

$$\begin{aligned} A_m(\theta) + iB_m(\theta) &= \frac{3}{4\pi\rho_e}\frac{1+k_n}{2n+1}\int_0^{2\pi}(\Delta I_n - \Delta\bar{I}_n)e^{im\lambda}d\lambda \\ \Delta C_{nm} + i\Delta S_{nm} &= \int_0^{\pi}(A_m(\theta) + iB_m(\theta))P_{nm}(\cos\theta)\sin\theta d\theta, \end{aligned} \tag{24}$$

where $[A_m(\theta), B_m(\theta)]$ are the interim variables solved in the first step and one can estimate the desired coefficients in the second step. Both steps are implemented using the Simpson quadrature formulation (Young & Gregory, 1988) since the input fields of this study are available on regular grids. In addition, spherical harmonic coefficients can be synthesized back to a pressure map p_{synt}, for visualizing the results in the next section as

$$p_{synt} = g_{wmo}\frac{a_e\rho_e}{3}\sum_n\sum_m\frac{2n+1}{1+k_n}P_{nm}(\cos\theta)(\Delta C_{nm}\cos m\lambda + \Delta S_{nm}\sin m\lambda), \tag{25}$$

where g_{wmo}, a_e and ρ_e refer to Table 2.

4 Results and discussions

Hourly atmosphere de-aliasing products of this study are computed up to degree and order 100 over the period of 2002 onwards. A separate set of tide byproducts including 12 tides in Table 1 is also computed. All the tidal and non-tidal products are called 'HUST-ERA5' hereinafter. Table 3 records the major differences among the HUST-ERA5, AOD1B-RL06 and ITG3D (Forootan et al., 2013) products, which construct the basis of our following assessments and discussions.

4.1 Fitted tides

The principal solar tides $[S_1, S_2]$ as well as ten smaller tides are computed over the period of 2007-2014, for keeping consistent with RL06 and enabling a comparison. Figure 4 takes the amplitude of $[S_1, S_2]$ as an example, and we can observe quite consistent spatial behaviors between the RL06 and HUST-ERA5, indicating that the contribution of S_1 and S_2 is quite similar within the two models. Specifically, the Pearson correlation analysis shows the value of 0.981 for S_1, and 0.996 for S_2. To further quantify the agreement, we use the 'misfit' as a measure of the relative differences between models $[model_I, model_{II}]$ as

$$Misfit = 100 \times RMS[model_I - model_{II}]/RMS[model_I], \tag{26}$$

where $RMS[.]$ means an overall Root Mean Squares (RMS) of gridded data for a given model. In this manner, misfit of S_1 derived between RL06 and HUST-ERA5 reaches up to

Table 3. A quick comparison between HUST-ERA5, AOD1B-RL06, and ITG3D products.

	HUST-ERA5	AOD1B-RL06	ITG3D
Input fields	ERA-5	ERA-interim, operational and forecast	ERA-interim
Sampling rate	1-hour	3-hours	6-hours
Integration method	SP+RVI[a]	SP+VI[b]	RVI[c]
Tide[d]	Removed	Removed	Not removed
IB effect	Corrected	Corrected	Not corrected
De-mean[e]	2007-2014	2007-2014	2001-2002

[a] denotes a combined surface pressure integration (SP) and refined vertical integration (RVI),

[b] denotes a normal vertical integration (VI),

[c] is another vertical integration method, see the Supporting Information Text.S1,

[d] includes 4 major tides $[S_1, S_2, S_3, M_2]$ as well as 8 minor tides $[P_1, K_1, N_2, L_2, T_2, R_2, T_3, R_3]$,

[e] denotes the time-mean that is removed from the time-series, see Eq. (23).

11.7%, and that of S_2 to 5.6%. A further analysis of the zonal averages shown in Figure 4(c) and (f) reveals that the differences are mainly distributed within the polar regions though they are generally small. These differences are probably caused by the differences between the atmospheric input fields used for producing the de-aliasing products. Other than $[S_1, S_2]$, a complete comparison of the 12 tides can be found in the Supporting Information Text.S1, where all the major tides (amplitude ≥ 10 [pa]) demonstrate a correlation coefficient higher than 0.9 between RL06 and HUST-ERA5.

4.2 HUST-ERA5 vs. RL06

Our study finds that the non-tidal component dominates (~10 times of the tidal component) the atmosphere variation, see the Supporting Information Text.S1. Therefore, in what follows we will focus on the analysis of non-tidal part of HUST-ERA5 and RL06. The dominant spatial-temporal changes of HUST-ERA5 are analyzed over the period of 2002-2020 in this section. For comparisons with RL06, we use the same truncation, i.e., at degree/order 100, and reduce the HUST-ERA5's sampling rate to 3 hours.

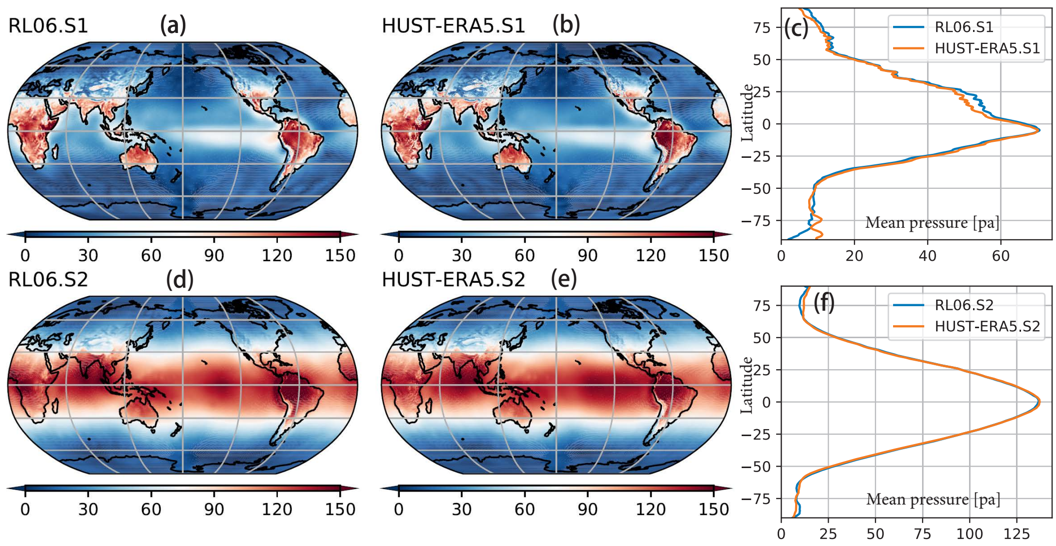

Figure 4. Comparisons of the tidal amplitudes (synthesized in pressure [pa]) derived from RL06 and HUST-ERA5 covering 2007-2014. The top two plots (a) and (b) demonstrate the amplitude of S_1 from RL06 and HUST-ERA5, respectively; (c) presents the zonally averaged S_1 amplitudes from both models; the bottom two plots (d) and (e) demonstrate the amplitude of S_2 from RL06 and HUST-ERA5, respectively; and (f) presents the zonally averaged amplitude of S_2 from both models.

As Dobslaw et al. (2015) discussed, the low-degree coefficients of de-aliasing products must be assessed as an index of data quality. For this, the degree-two coefficients $[C20, C21, C22, S21, S22]$ during 2019 are shown in Figure 5 as an example. We do not compare the degree-one coefficients since they are usually ignored or replaced in the GRACE gravity field inversion (Flechtner et al., 2014) and GRACE applications (Loomis et al., 2020). Plots in Figure 5(a-e) indicate a very close correspondence between HUST-ERA5 (marked in the black solid line) and RL06 (marked in the red dashed line). A detailed statistical analysis of our comparisons is reported in Table 4.

To explore the dominant spatial-temporal patterns of the atmospheric mass changes, the Principal Component Analysis (PCA, Forootan, 2014, chapter 3) is applied to the dataset of 2002-2019, and the results are presented in Figure 6. It should be mentioned here that, before applying PCA, both RL06 and HUST-ERA5 are temporally averaged to produce monthly means. By this, the differences between the two products can be better related to possible impacts on the level 2 gravity products (see e.g., Forootan et al., 2014). The

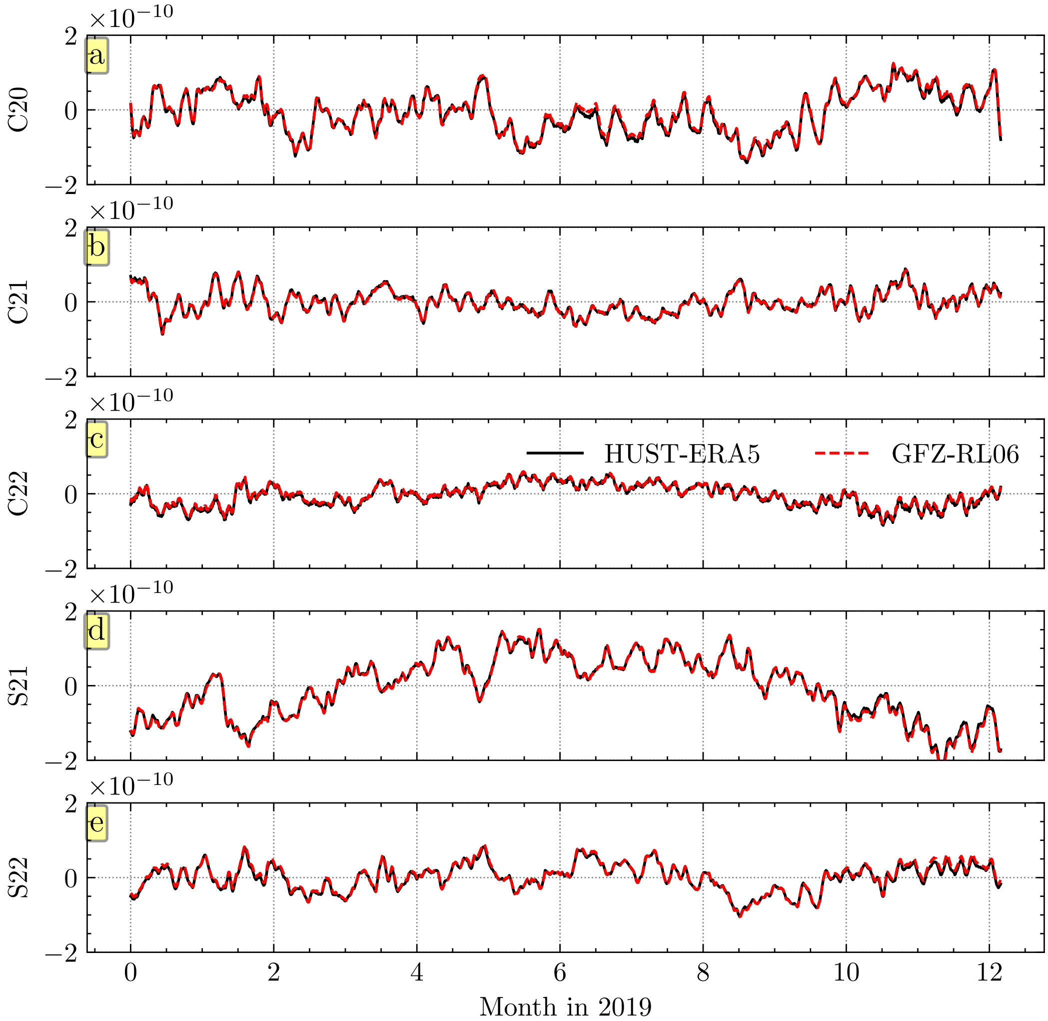

Figure 5. Time series of degree-two coefficients [dimensionless] of HUST-ERA5 and RL06 during 2019. From top to bottom, (a-e) show the time series of $C20$, $C21$, $C22$, $S21$, and $S22$, respectively.

spatial anomalies are synthesized back to the equally-spaced $1^\circ \times 1^\circ$ surface pressure fields using Eq. (25).

The Empirical Orthogonal Functions (EOFs) derived from PCA denote the dominant mutually orthogonal spatial anomalies that correspond to uncorrelated Principal Components (PCs). In Figure 6, the EOFs as well as the PCs are sorted with respect to their variance contributions from big to small. The top four components of either HUST-ERA5 or RL06 contribute to 81.9% of the total variance. Moreover, the EOF1 and PC1 of both products represent more than 50% of the variance, i.e., 55.4% and 56.5% for HUST-ERA5 and RL06, respectively, see Figure 6(a) and (e). Pearson correlation analysis indicates a high

Table 4. A statistical analysis of the low-degree coefficients of HUST-ERA5 and RL06 during 2019. Note that RMS1 [dimensionless, $\times 1e^{-9}$] indicates the Root Mean Squares (RMS) of HUST-ERA5, and RMS2 [dimensionless, $\times 1e^{-9}$] indicates that of RL06. The calculation of the misfit is derived from Eq. (26).

Coeff	Correlation	RMS1	RMS2	Misfit
C_{20}	0.997	2.135	2.106	10.1%
C_{21}	0.998	1.155	1.124	7.0%
C_{22}	0.997	1.121	1.066	13.8%
C_{30}	0.999	3.115	3.211	4.6%
C_{40}	0.996	1.354	1.419	12.7%
C_{50}	0.998	1.105	1.170	8.8%
S_{21}	0.999	2.768	2.688	9.7%
S_{22}	0.997	1.071	1.027	9.8%
S_{31}	0.999	2.058	2.039	6.0%
S_{41}	0.999	1.345	1.344	7.0%
S_{51}	0.998	1.025	1.018	7.0%

correlation coefficient (0.98) between EOF-1 of both products. In addition, the remaining three EOFs also demonstrate high correlation coefficients (all > 0.95) and similar variance contributions (HUST-ERA5: $[17.2\%, 6.2\%, 3.1\%]$; RL06: $[16.4\%, 6.0\%, 3.0\%]$).

By analyzing the PCs of Figure 6(i), (j), (k), and (l), it can been seen that, unlike RL05, no apparent jump is found in RL06 and HUST-ERA5 anymore (Duan et al., 2012; Forootan et al., 2014), showing a better long-term stability of the atmospheric input fields used by RL06 and HUST-ERA5 over that by RL05. In addition, no cyclic evolution close to tidal frequencies can be found in the PCs showing that these components are correctly removed. Comparing the two products, it can be seen that the HUST-ERA5 (solid blue curve) are mostly overlapping RL06 (dashed orange curve) for all the four PCs. The misfits in a definition by Eq. (25) for the four PCs are respectively 10.5%, 14.2%, 13.8% and 21.3%, suggesting that two products are comparable in terms of time-series. But meanwhile, the differences are still distinguished and require to be further quantified. To this end, we plot the PCA of the differences between these two time-series in Figure 7.

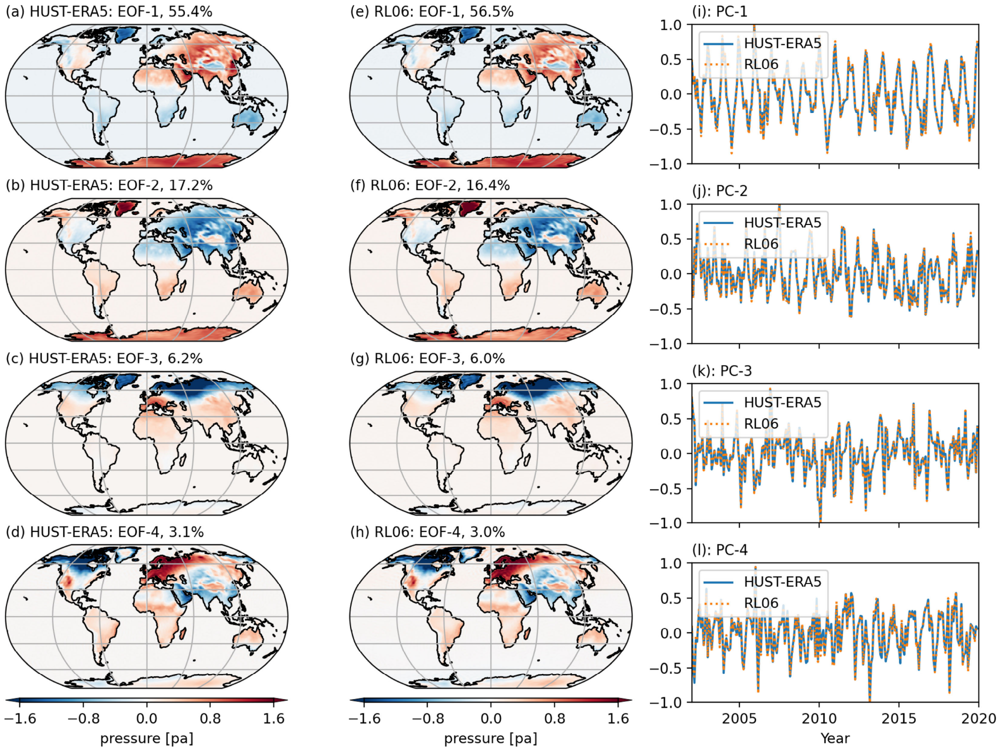

Figure 6. PCA results of time series of two products (HUST-ERA5 and RL06) during 2002-2020. From top to bottom, the plots represent the orthogonal modes arranging with decreasing their contribution in the total variance. Plots on the left (a, b, c, and d) are the EOFs of HUST-ERA5, while those in the middle (e, f, g, and h) correspond to RL06. Their PCs are shown in (i, j, k, and l), respectively. In this presentation, EOFs and PCs are rescaled to have the same range to enhance the comparisons.

According to Figure 7, the leading four EOFs represent over 60% of the total variance, of which EOF-1 dominates the differences (39.8%). EOF-1 manifests a fairly uniform spatial distribution, i.e., an ascending difference with increasing latitude, implying a suspicious systematical bias that probably introduced by the computation method since differences of input fields are more likely randomly distributed. The corresponding PC-1 demonstrates that such a bias between HUST-ERA5 and RL06 contains inter-annual fluctuations. Therefore, special care should be taken for applications of de-aliasing product on inter-annual signal interpretations over high-latitude regions, in particular at Greenland and Antarctica. For instance, the uncertainty of GRACE derived inter-annual mass fluctuation over the polar regions should be updated by accounting for the bias in the atmospheric de-aliasing modelling, see e.g., Forootan et al. (2014). In addition to the first mode, PC-4 in Figure 7

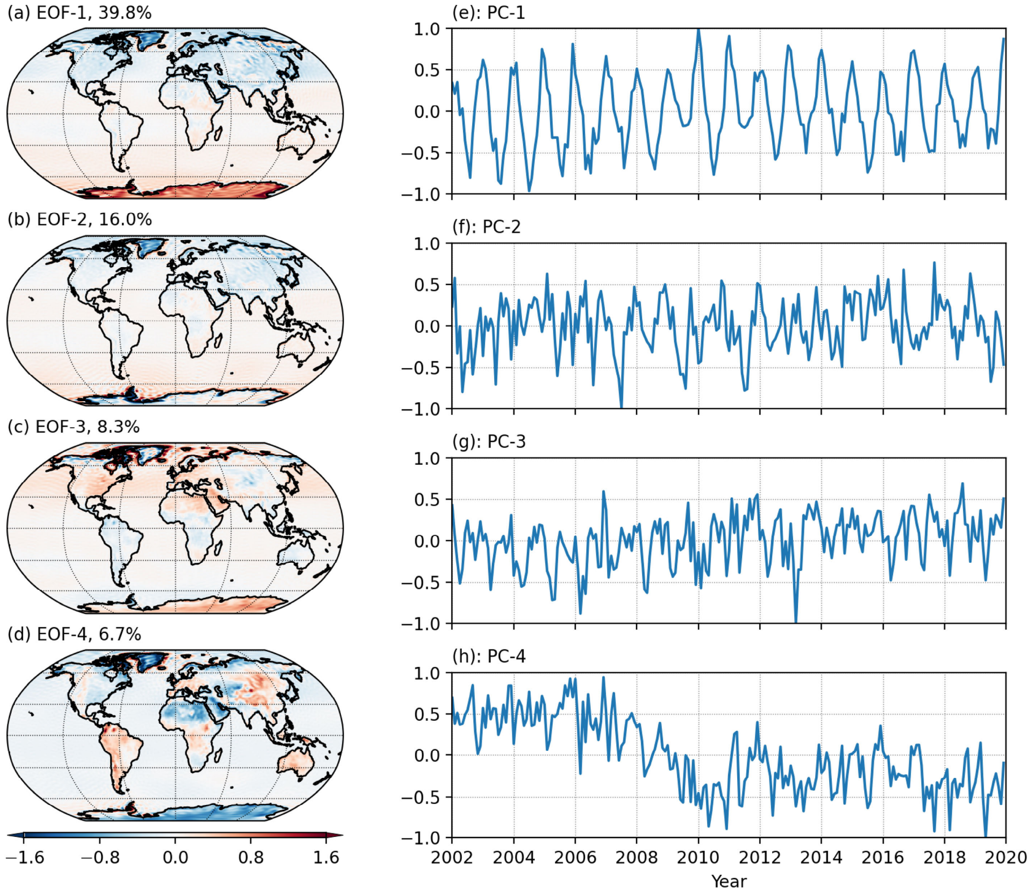

Figure 7. PCA results of the differences (HUST-ERA5 minus RL06) during 2002-2020. From top to bottom, the plots represent the orthogonal modes arranging with decreasing their contribution in the total variance. Plots on the left (a, b, c, and d) are the EOFs, and their corresponding PCs are shown in (e, f, g, and h) on the right, respectively.

reveals another prominent and suspicious 'jump' manifested as a sudden drop at year 2007, which remains to be explained. The reason can be found in the RL06's technical document, where a switch of input fields from ERA-interim reanalysis to the operational data in 2007 is reported, which we think leads to the 'jump' in PC-4. And this is not one occasion, since another ambiguous 'jump' is visible at 2010 as well, where the horizontal resolution of operational data was greatly improved at that time according to Dobslaw et al. (2017a). These changes have been well captured and reflected by the 'jumps' in PC-4, indicating a slightly better consistency of HUST-ERA5 over RL06, in particular in Greenland and Antarctica as shown by EOF-4 in Figure 7(d).

In summary, HUST-ERA5 and RL06 have shown a fairly comparable performance in terms of time-series analysis, however, their discrepancy is sill non-negligible and remains to be studied, see the misfit of low-degree comparison (Table 4) and PCA differences (Figure 7). In this sense, we make a further analysis of possible factors that may lead to the discrepancy in the following sections, from the perspective of input fields, integration method and sampling rate as shown in Table 3.

4.3 Input fields: ERA-interim vs. ERA-5

In this section, we test the input fields on the estimation of atmospheric de-aliasing products. After 2007, RL06 adopted operational analysis data that is inaccessible otherwise, making it impossible to directly assess the input fields from 2007 onwards. However, ERA-interim is employed for RL06 priori to 2007, which is publicly available. Therefore, the following assessment of input fields are made between HUST-ERAI (modeled with ERA-interim) and a particular HUST-ERA5. Such a HUST-ERA5 is produced with down-sampled 6-hourly ERA5 for comparing ERA-interim. In addition, HUST-ERAI and HUST-ERA5 are both computed for a full year across 2006, following the method in Eq. (22) and Eq. (23), albeit without tide removal nor IB-correction as shown by Eq. (5) and Eq. (7) since this is only a comparison.

An arbitrary selected scenario at 2006-01-06 00:00:00 is first studied in Figure 8(a), where we calculate the degree variance of the geoid height (see., Swenson & Wahr, 2002) from the spherical harmonic coefficients of HUST-ERAI (in red) and HUST-ERA5 (not shown), respectively. Their differences are plotted in black dashed line to compare with GRACE prelaunch accuracy (Kim, 2000) in green solid line, as well as a simulated accuracy (in blue solid line) of Bender-type constellation (Gruber, 2010) that is the most desired option for the next generation gravity mission. It can be found from Figure 8(a), even a simple switch of input fields has already led to a difference beyond the GRACE-prelaunch accuracy, without mentioning the Bender-type. In fact, the actual error of de-aliasing is supposed to be much larger, and the black dashed line only represents the model difference instead of the actual error. In this experiment, changing the input fields mainly affect the GRACE prelaunch accuracy less than d/o 12 (see the cross of green curve and black dashed line), however, this influence can't be sensed by the current GRACE(-FO) since it is still lower than the present GRACE calibration error (Poropat et al., 2019). The spectral differences (in black dashed line) are further converted into spatial difference in terms of the geoid height as shown in

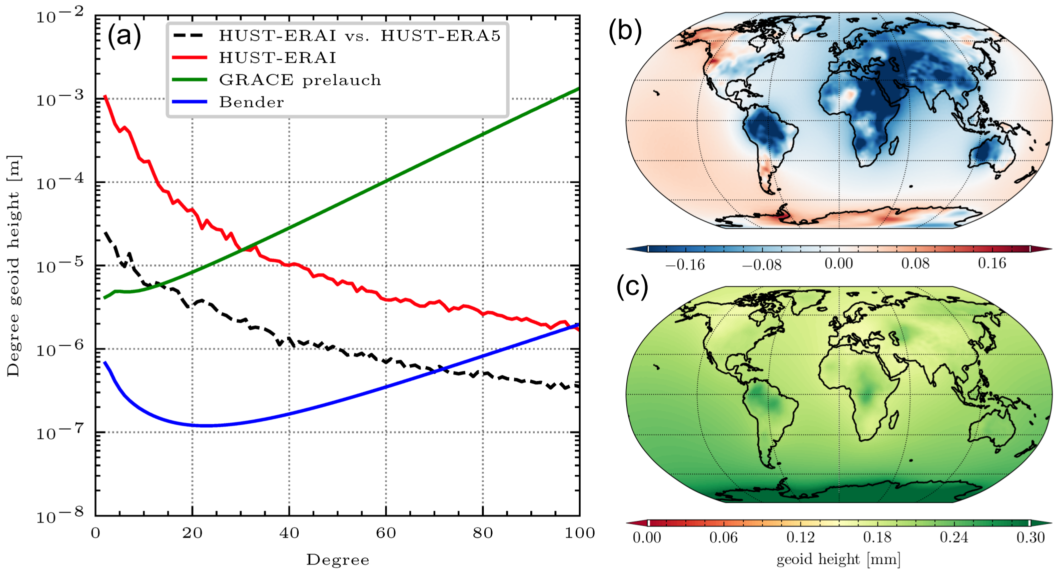

Figure 8. Comparisons between de-aliasing product using input fields ERA-interim and ERA-5: (a) spectrum analysis in terms of degree variance of the geoid height [m], compared to GRACE prelaunch accuracy (in green) as well as the planed Bender-type accuracy (in blue). (b) a snapshot of spatial difference at 2006-01-06 00:00:00, in terms of geoid height [mm]; (c) RMS of temporal geoid height difference for a full year. Note that label 'vs' hereinafter denotes the model difference unless special statement.

Figure 8(b), where a global variation in amplitude of 0.2 mm is manifested. Such a variation should be accounted for a planned gravity mission that expects to acquire millimetre geoid height accuracy. In addition to the test on single epoch, Figure 8(c) calculates the point-wise temporal RMS for a full year to assess performance of the time-series, as done before in Boy and Chao (2005). Figure 8(c) reveals an apparent global variation of the geoid height in the amplitude of ∼0.3 mm, of which the peak is nevertheless reached over Antarctica. The mass anomaly over Antarctica remains as a question that is subject to further study. Above spectrum and spatial difference can somewhat represent the contribution of input fields to the difference between HUST-ERA5 and RL06.

4.4 Inner integral: RVI vs. NVI

In summary, the refinements relative to the NVI (see Section 3.5) of RL06 are made from three aspects: (i) geometrical refinement with geoid undulation considered, (ii) physical refinement with point-wise gravity accelerations introduced, and (iii) numerical refinement with a linear interpolation of the fields (temperature, humidity and pressure). To enable a comparison, we respectively use NVI and RVI methods to generate two sets of atmospheric de-aliasing products, based on nevertheless the same input fields ERA-5 for a 3-month period from January to March 2017.

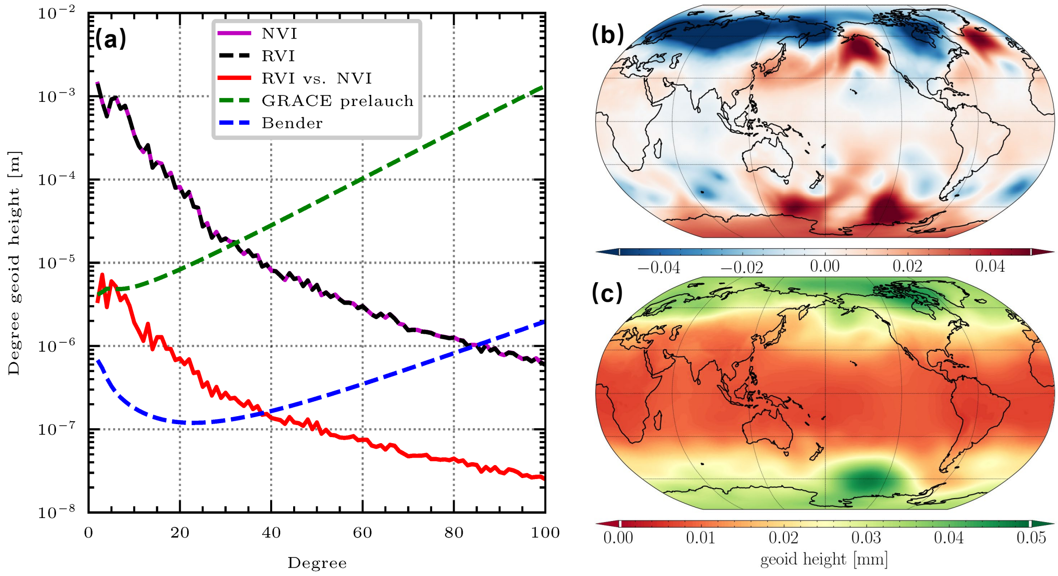

Figure 9. Comparisons between de-aliasing product using NVI and RVI method: (a) spectrum analysis in terms of degree variance of the geoid height $[m]$, compared to GRACE prelaunch accuracy (in green) as well as the planed Bender-type accuracy (in blue). (b) a snapshot of spatial difference at 2017-01-07 12:00:00, in terms of geoid height $[mm]$; (c) RMS of temporal geoid height difference for a three-months period.

Figure 9(a) shows the degree spectrum of the geoid height at an arbitrary epoch 2017-01-07 12:00:00. As done before, GRACE prelaunch accuracy as well as Bender-type design accuracy is again plotted as the reference. The differences (in red solid line) between the NVI and RVI are shown to be much smaller than the expected GRACE accuracy (in green dashed line), with a comparable level at the very-low degree less than 5 corresponding to a spatial wavelength of 7200 km or larger. Such an impact is obviously smaller than that shown in Figure 8(a), probably inferring that computation method's contribution is less than input fields. Nevertheless, when compared to the Bender's expected accuracy, the red curve stands still higher than the blue dashed line priori to degree 40, showing its value on possible future gravity mission. Another verification is made on the spatial performance in terms of single-epoch and a three-month time-series (Jan 2017 to Mar 2017), see Figure 9(b-c). Despite that this computation method's contribution (amplitude up to $\sim$0.05 mm) is less than that of the input fields, Figure 9(b-c) demonstrate an obvious latitude-dependant effect that probably corresponds to the principal EOF-1 in Figure 6(a). However, one may pose question that the difference shown by RVI vs. NVI is very small while EOF-1 is significant on the contrary. We suppose it from three aspects, (i) NVI used in RL06 is quite advanced and the improvement brought by RVI can not be significant, unlike the considerable difference between vertical integral and surface integral found by Boy and Chao (2005); Swenson and Wahr (2002); (ii) NVI and RVI compared in this study are both configured with common parameters defined in Table 2 as well as the same related formulations, whereas these might be slightly different from RL06's setup that we do not know; (iii) a coupling of the computation method and input fields will amplify the influences. Anyhow, we think the computation method will lead to a bias of de-aliasing modelling regardless of its magnitude. This is again confirmed by another detailed analysis of the individual contribution of the geometrical, physical and numerical method refinements, please refer to the Supporting Information Text.S2. Through this analysis, we additionally identify the physical refinement as the main contributor of such a systematic bias on de-aliasing modelling.

4.5 Temporal resolution: 6hr vs. 3hr vs. 1hr

Practical use of the de-aliasing product in GRACE gravity field inversion requires a substantial linear interpolation to keep synchronization with other instruments, i.e., 5-second SCA (star camera for measuring satellite's attitudes, 1-second for GRACE-FO). Therefore, impact of the de-aliasing product's time-resolution on the interpolation as well as on the gravity inversion deserves to be studied. To this end, HUST-ERA5 are re-sampled into 1-hour, 3-hours and 6-hours respectively to enable comparisons. Note that, the comparisons are made by always interpolating the product of lower sampling rate into a higher one. For instance, if we anticipate to study 'HUST-1hr versus HUST-3hr' at an epoch 13:00:00 of 2018-01-01, the time-series of HUST-3hr has to be linearly interpolated between epochs 12:00:00 and 15:00:00 to derive the value at 13:00:00. The process is similar for 'HUST-3hr versus HUST-6hr', the time-series of HUST-6hr is linearly interpolated between epochs 12:00:00 and 18:00:00 to reach the value at 15:00:00, so that the comparison to HUST-3hr is enabled.

In this way, we firstly plot the degree variance of two scenarios (HUST-3hr versus HUST-1hr, and HUST-6hr versus HUST-3hr) in Figure 10(a). As a reference, the degree

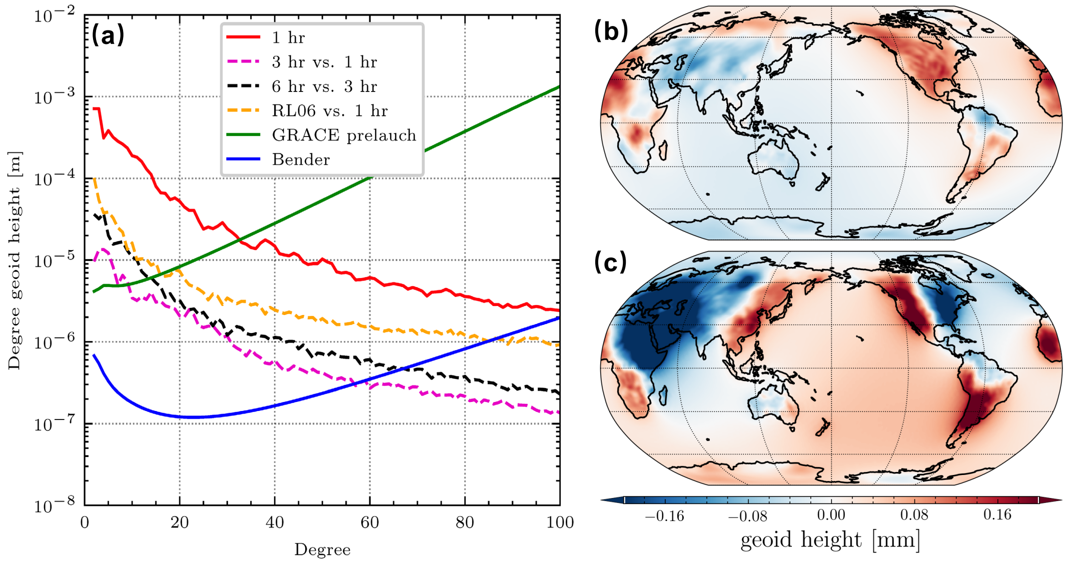

Figure 10. Spectrum (a) and spatial (b-c) performances of the de-aliasing products HUST-1hr, HUST-3hr and HUST-6hr: (b) gives a snapshot of HUST-1hr versus HUST-3hr (linearly interpolated) at 2018-01-01 13:00:00, in terms of geoid height [mm], and (c) denotes HUST-3hr versus HUST-6hr (linearly interpolated) at 2018-01-01 15:00:00.

variances of HUST-1hr and 'HUST-1hr versus RL06' are plotted as well. In addition, the GRACE prelaunch accuracy and Bender-type accuracy are shown in Figure 10(a) as we did before. It can be seen from Figure 10(a) that, the black dashed line stays much higher than the purple dashed line over all the spectrums, demonstrating that the impact caused by '3hr versus 1hr' is lower than that by '6hr versus 3hr'. The black dashed line affects the GRACE prelaunch accuracy prior to degree and order 17, whereas the purple dashed line has only an impact prior to degree and order 9. Correspondingly, their spatial performances are also revealing the same phenomenon, see Figure 10(b-c). Statistically, Figure 10(b) has a magnitude of only 0.084 mm over 70 percentage of the continent, whereas Figure 10(c) amounts to 0.175 mm.

The finding that '6hr versus 3hr' has a greater significance than '3hr versus 1hr' is not one occasion but can be again confirmed by their RMS maps across a full year test, see Figure 11(a-b). As shown by Figure 11, the RMS map of '3hr versus 1hr' has an apparent smaller magnitude than that of '6hr versus 3hr' all over the globe. Statistically, Figure 11(a) has a magnitude of $\sim$0.1 mm over 50 percentage of the continent except for the polar regions, whereas Figure 11(b) amounts to only $\sim$0.05 mm. As a summation, the temporal change

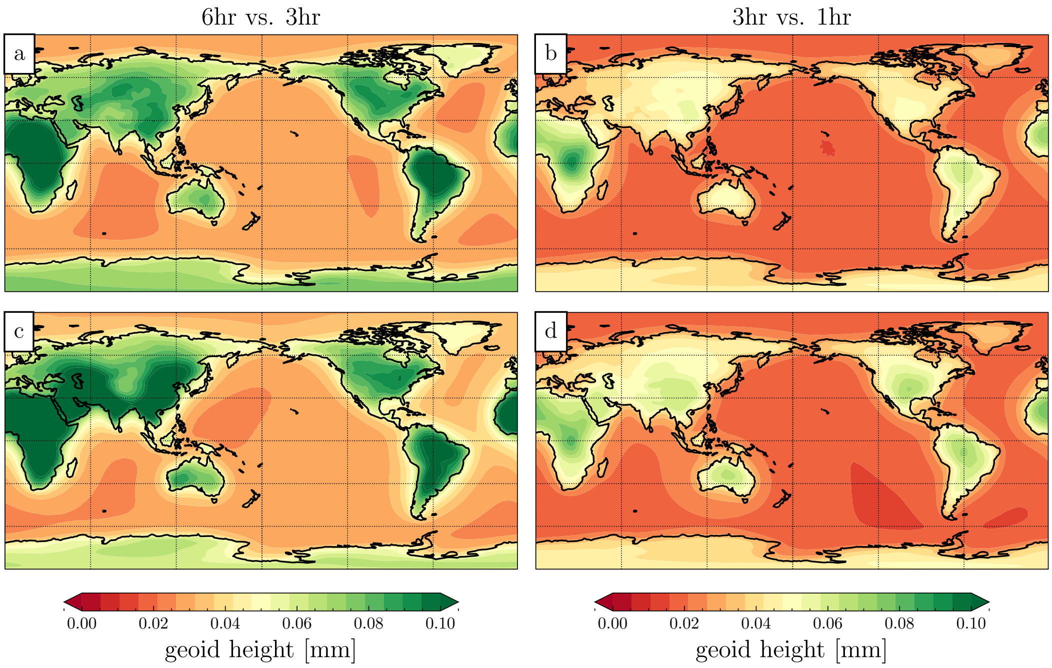

Figure 11. The RMS of temporal geoid height differences for a one-year period (2018). Plots (a) and (c) denote the scenario of HUST-6hr versus HUST-3hr, while (b) and (d) denote HUST-3hr versus HUST-1hr. In particular, the top row (a,b) removes all the 12 tides, whereas the bottom row (c, d) removes only $[S_1, S_2]$ tides as a reference.

from 6 hour to 1 hour will lead to RMS up to $\sim$0.15 mm (the median value). Note that the RMS maps shown in Figure 11(a-b) are the results with a removal of all tides. In order to investigate the possible influence of tide removal on the temporal resolution, we calculate another one-year RMS for the corresponding scenario where 10 small tides are retained, see Figure 11(c-d). Contrasting the top and bottom rows in Figure 11, we find the coupling effect brought by remaining 10 small tides does exist, for instance, deviations between Figure 11(a) and Figure 11(c) are distinguished over the Europe and Asian. However, the effect is not that significant, since the top and bottom rows in Figure 11 demonstrate an overall comparable spatial performance over majority of the continents. This is reasonable because the tidal components are much smaller than the non-tidal components, see also in the Supporting Information. Nevertheless, we still suggest removing all the tide lines to prevent the coupling effect when changing the temporal resolution, in particular for the case of 6hr versus 3hr, see Figure 11(a) and Figure 11(c).

At last, both Figure 10 and Figure 11 reveal that, the temporal resolution's impact has already exceeded the impact of method change (Figure 9), and it is only slightly lower than that of the input fields, see Figure 8. In particular, the black dashed line in Figure 10(a) is quite close to the orange dashed line that denotes the case of RL06 versus HUST-1hr. All these findings may suggest the significance of improving the temporal resolution when generating the AOD products. Nevertheless, we have to also realize that, the impact by improving the temporal resolution (either 3-hr or 1-hr) is still below the current GRACE(-FO) accuracy from the view of degree geoid height. The added value of the temporal resolution's change might be only expected for the NGGM of Bender-type, in this sense. But with the continuous improvement of L1b data processing technology, its significance is also likely found by the GRACE(-FO), since the black curve has greatly surpassed the GRACE prelaunch accuracy, see Figure 10(a). Therefore, we suggest generating an 1-hourly AOD product to be tested in the processing chain of GRACE-FO before being used for operational NGGM.

4.6 A case study for GRACE-FO

HUST-ERA5, as an alternative atmosphere de-aliasing product to the official RL06, can be also used to evaluate the impact of de-aliasing models on GRACE-FO. In this section, we carry out such an evaluation by comparing HUST-ERA5 (of different temporal resolution) with RL06 in terms of GRACE-FO orbit integration as well as the low-low tracking data.

As of now, the demonstrated experiment in Figure 10 is based on a single epoch, e.g., 13:00:00, whereas the linear interpolation in practice for GRACE(-FO) orbit determination or Earth gravity recovery is made for every 5 seconds (GRACE case) or 2 seconds (GRACE-FO case). The net impact of temporal resolution across a given time period like an arc of 24 hours can be hardly represented in the way of Figure 10. To this end, we respectively use the HUST-1hr, HUST-3hr and HUST-6hr as the background model to implement an orbit integration with a 24-hours arc and a step length of 2 seconds. All the conservative and non-conservative force models have been considered (see Yang et al., 2017), associated with GRACE-FO level-1b instrument data described already in Section 2. We hope, in this way, to precisely quantify the impact of model's temporal resolution with the final orbit differences, see Figure 12. In addition, the effect of atmosphere tidal constitutes S_1 and S_2 are provided as benchmarks, since the atmospheric tides are usually assumed as the smallest force model that has to be considered in the precise orbit determination (POD) as well as precise temporal gravity determination (see Lasser et al., 2020).

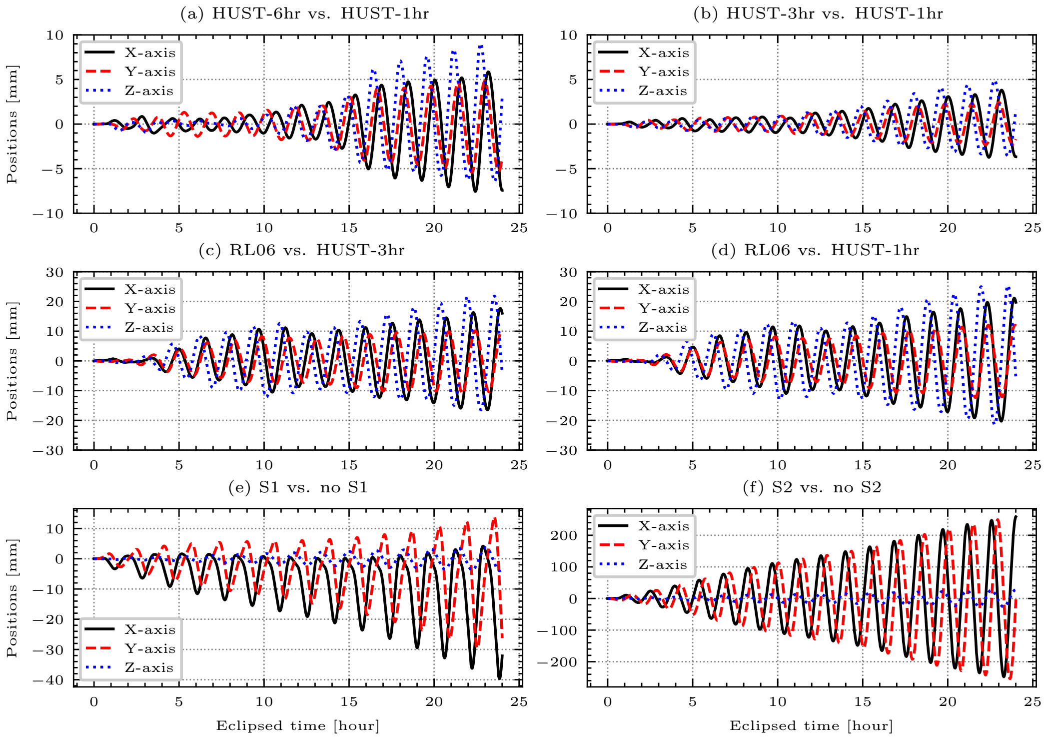

Figure 12. Comparisons of atmospheric de-aliasing products in terms of 3-axis orbit propagation differences, choosing a 24-hours arc of GRACE-FO located at 2019-01-06 as an example. Plot (a) describes a scenario of HUST-6hr versus HUST-1hr, denoting that the orbit propagations are compared between that with HUST-6hr and with HUST-1hr. The subsequent plots (b)(c)(d) are using the same convention as (a). Similarly, (e)(f) describe scenarios of orbit propagation comparisons between that with atmospheric tide $S_1(S_2)$ and without $S_1(S_2)$.

Here, the magnitude of final orbit difference (see the end of the plots) representing the POD error is regarded as an indicator of force model's influence. In this way, the error caused by HUST-6hr is found to be almost twice as much as that of HUST-3hr by contrasting Figure 12(a) with Figure 12(b), suggesting that a lower sampling rate will cause a larger orbit discrepancy. In particular, the error of 'HUST-6hr versus HUST-1hr' has reached $\sim 2\ cm$ after an orbit propagation of 24 hours, and this impact might be worthy of consideration for the GRACE-FO POD that asks for centimeter precision. Besides, Figure 12(b) also amounts to $\sim 1\ cm$. This is to say, their influences are all on the order of centimeters, demonstrating the significance of improving de-aliasing product's temporal resolution. In addition, Figure 12(c-d) compares the RL06 with HUST-3hr (HUST-1hr), where the magnitude of final orbit difference approaches $\sim$4 cm that is entirely comparable to S_1, despite that the impact is still much less than that of S_2, see Figure 12(f). Therefore, we think, the difference of 1-hourly HUST-ERA5 from RL06 is remarkable and should be accounted for the POD of GRACE-FO, otherwise the usage of atmospheric tide S_1 makes no sense neither.

We also notice that, some attempts were made to connect the force model evaluation with GRACE intersatellite tracking measurements, such as the KBR(R)-residual (K-band ranging residuals or ranging-rate residuals), see Han et al. (2009); Dobslaw et al. (2017b); Yang et al. (2018). This is feasible because the force model differences, which are hardly distinguished by monthly mean gravity fields due to the downward continuation and filtering process, are now possible to be revealed by KBRR-residual analysis. Nevertheless, rather than the KBRR-residual, this study will leverage the rstever laser ranging interferometer (LRI) measurements acquired by GRACE-FO, to quantify the impact of atmospheric de-aliasing products. Ghobadi-Far et al. (2020) recently finds that LRI captures gravitational signals as small as 0.1 nm/s^2 at 490 km altitude, improved by one order of the magnitude from KBR. This allows LRI to uniquely detect un/mismodeled background force models, e.g., the possible error/bias in the atmospheric de-aliasing products.

In this study, the LRI range-rate residuals at a sampling rate of 2 seconds are acquired and analyzed for one-month (January 2019) GRACE-FO level-1b data, by applying HUST-1hr, HUST-3hr, HUST-6hr and RL06 respectively. The computations are done for all cases with the ocean de-aliasing omitted, while keeping the rest force models unchanged. Comparison of LRI range-rate residual for every case is made against the HUST-1hr, see in Figure 13. HUST-1hr is chosen as the baseline since it has the highest sampling rate. For a straight-forward impression, the complete records of LRI range-rate residuals for one single day are first presented in Figure 13(a-c). Obviously, the green curve shown in Figure 13(b) varies more sharply than the black in Figure 13(a). Statistically, the RMS of black curve approximates to 1.51 nm/s, whereas the RMS of green approximates to 2.47 nm/s that is $\sim$1.6 times that of the black. This implies that the temporal resolution reduction from 1 hour to 6 hours would lead to a larger LRI range-rate residuals. When extending the one-day result to the whole month (because the temporal gravity field is acquired as a monthly mean at present), the mean RMS of green (HUST-1hr versus HUST-6hr) approximates to 2.19 nm/s, see Figure 13(d). Correspondingly, the mean RMS of black (HUST-1hr versus

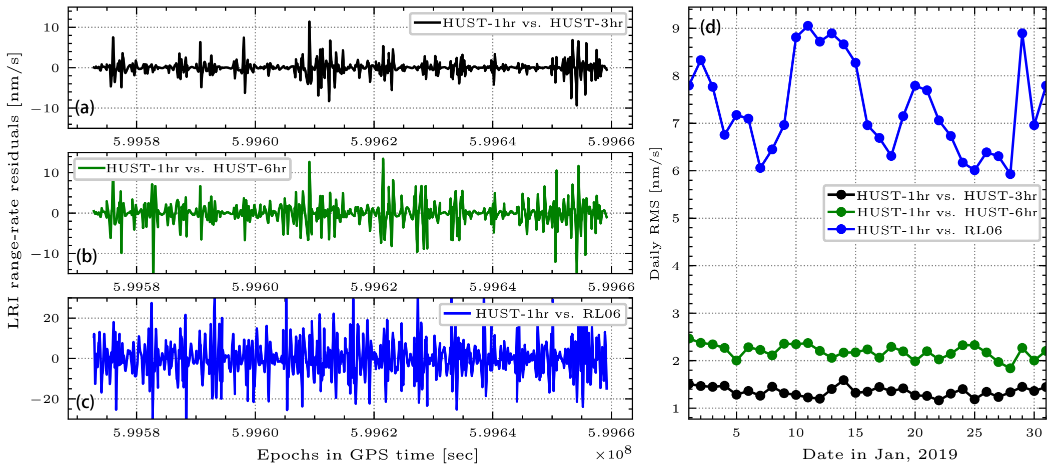

Figure 13. Performance of various atmospheric de-aliasing products in terms of LRI range-rate residuals [nm/s]. (a)(b)(c) respectively represent the cases of HUST-3hr, HUST-6hr, RL06 against HUST-1hr in 2019-01-01. The x-axis denotes the GPS time within the specified day, at a sampling rate of two seconds. (d) summarizes the daily RMS of LRI range-rate residuals for each case given in (a)(b)(c) throughout the whole January of 2019.

HUST-3hr) approximates to 1.35 nm/s, which is also $\sim$1.6 times that of the green curve. This consistent performance between daily and monthly results further confirms that, the reduction of temporal resolution would deteriorate the LRI range-rate residuals at an order of 1.35$\sim$2.19 nm/s. The recent study of Abich et al. (2019) by analyzing the in-orbit performance of GRACE-FO LRI concludes that, the LRI noise is well below the requirement, reaching 10 $nm/\sqrt{Hz}$ at 40 mHz and 300 $pm/\sqrt{Hz}$ at 1 Hz. After a simple translation (multiplied with $2\pi f$), the LRI range-rate precision is estimated to be within 1.9$\sim$25 nm/s. In this context, the temporal resolution's impact (1.35$\sim$2.19 nm/s) is quite close to the LRI precision.

Figure 13(c) records the differences of LRI measurements between HUST-1hr and RL06 as well, where the magnitude of time-series variation (blue curve) has largely exceeded that in Figure 13(a)(b). Statistically, its RMS approximates to 7.80 nm/s. As for its performance in the whole month, the mean daily RMS approximates to 7.34 nm/s that is much greater than 1.35 nm/s and 2.19 nm/s, indicating a more significant influence caused by the input data (ERA-5) than the temporal resolution. This conclusion is also consistent with the previous results. In particular, as the monthly mean difference 7.34 nm/s of LRI range-rate residuals is beyond the LRI precision, a consideration of 1-hourly ERA-5 reanalysis to produce a new de-aliasing modelling is suggested for the next-generation gravity missions, to exploit the high-precision on-board LRI instrument.

5 Conclusion

This study takes advantage of the newly available global climate data ERA-5, and successfully combines the RL06 method with proposed refinements to realize a new non-tidal atmospheric de-aliasing product called HUST-ERA5. HUST-ERA5 differs with the official RL06 product at three main aspects: (i) the latest high-quality long-term reanalysis ERA-5 is used in HUST-ERA5, whereas ERA-interim along with the operational analysis dataset is the major resource of RL06, (ii) HUST-ERA5 has considerably improved the temporal resolution from 3-hours to 1-hour, (iii) a refinement with physical, numerical and geometrical modification on the RL06's computation is facilitated in HUST-ERA5. Extensive comparisons among the RL06, HUST-ERA5 and reduced time-resolution HUST-ERA5 (3 hours/6 hours) has found that, the input fields as shown by (i) have a dominant impact on the quality of atmospheric de-aliasing product, followed by (ii) and (iii) if sorted by the magnitude of their contribution. In particular, the impact caused by (i) and (ii) is close to or beyond the precision of GRACE-FO LRI instrument, and therefore should be taken into account for the design of next-generation gravity mission that is supposed to carry a same or more sensitive LRI instrument. Besides, a better long-term consistency could be expected from HUST-ERA5 with respect to RL06 (a minor jump over 2007 is found), because of the continuous ERA-5 dataset. We also note that, a suspicious systematical bias caused by different integration methods is found at high-latitude regions, which should be taken care in science applications of GRACE to interpret, i.e., the uncertainty of ice-sheet mass balance. Nevertheless, no significant impact of these differences between HUST-ERA5 and RL06 is visible for the present GRACE and GRACE-FO through our analysis. As a summary, HUST-ERA5 has fulfilled a comparable and consistent modeling quality as RL06, while an added value on future satellite gravity mission might be anticipated from HUST-ERA5 because of the ERA-5's better quality and consistency, as well as higher temporal resolution. Therefore, we believe that HUST-ERA5, including the tidal product $[S_1, S_2]$ and others, is qualified and could be considered as an alternative choice other than the official RL06 for Earth gravity recovery in the GRACE(-FO) community.

Despite the demonstrated advances already obtained with ERA-5, several extensions are applicable in the future research. One possible extension is quantifying the uncertainties of variables provided by ERA-5, which is critical for the simulation work for next-generation gravity mission. This might be addressed through an inter-comparison among the current reanalysis products such as MERRA-2, JRA-55 and even the upcoming CRA-40 from China. Another possible extension could be a further study on ocean de-aliasing by running specific OGCM (Oceanic General Circulation Model) to acquire a complete atmosphere and ocean de-aliasing product. A particular OGCM, such as Chinese LICOM model (Liu et al., 2014), may have considerable improvements regionally, which is subject to our future studies.

Acknowledgments

The authors acknowledge financial supports through the National Natural Science Foundation of China (Grant No.41804016, No.41931074 and No.41704013), and National Key Research Development Program of China with project No.2018YFC1503503. The authors state that all the data in this study are publicly available. GRACE level 1B data as well as the AOD1B-RL06 are obtained from GFZ data center (`ftp://isdcftp.gfz-potsdam.de/grace-fo/`). ERA-interim and ERA-5 data used in this study are publicly available from ECMWF (`https://www.ecmwf.int/en/forecasts/datasets/browse-reanalysis-datasets`). Our new atmospheric de-aliasing product HUST-ERA5 can be downloaded from a verified data storage site (National Tibetan Plateau Data Center, China, doi: 10.11888/Geo.tpdc.271147). The ocean mask used in this study and the derived 12 tides can be also downloaded from the figshare site (`https://doi.org/10.6084/m9.figshare.14113010.v1`). The authors would like to thank editor and the reviewers for their helpful comments.

References

Abich, K., Abramovici, A., Amparan, B., Baatzsch, A., Okihiro, B., Barr, D., . . . Zimmermann, M. (2019, 07). In-Orbit Performance of the GRACE Follow-on Laser Ranging Interferometer. *Physical Review Letters*, *123*. doi: 10.1103/PhysRevLett.123.031101

Barthelmes, F. (2013). Denition of Functionals of the Geopotential and Their Calculation from Spherical Harmonic Models. *GFZ Scientic Technical Report*. Retrieved from `www.gfz-potsdam.de` doi: 10.2312/GFZ.b103-0902-2

Behzadpour, S., Mayer-Grr, T., Flury, J., Klinger, B., & Goswami, S. (2019, 08). Multiresolution wavelet analysis applied to GRACE range-rate residuals. *Geoscientific Instrumentation, Methods and Data Systems*, *8*, 197-207. doi: 10.5194/gi-8-197-2019

Berrisford, P., Dee, D., Poli, P., Brugge, R., Fielding, K., Fuentes, M., . . . Simmons, A.

(2011, 11). The ERA-interim archive: Version 2.0. *ERA Report Series*, *1*.

Biancale, R., & Bode, A. (2006). Mean annual and seasonal atmospheric tide models based on 3-hourly and 6-hourly ECMWF surface pressure data. *Scientific Technical Report STR; Potsdam: Deutsches GeoForschungsZentrum GFZ*.

Boy, J.-P., & Chao, B. F. (2005). Precise evaluation of atmospheric loading effects on Earth's time-variable gravity field. *Journal of Geophysical Research: Solid Earth*, *110*(B8).

Butterworth, S. (1930). In the theory of filter amplifires. *Experimental Wireless and the Wireless Engineer*, *7*.

Cambiotti, G., Douch, K., Cesare, S., Haagmans, R., Sneeuw, N., Anselmi, A., ... Sabadini, R. (2020, 07). On earthquake detectability by the next-generation gravity mission. *Surveys in Geophysics*, 1-26. doi: 10.1007/s10712-020-09603-7

Chao, B. F. (2005). On inversion for mass distribution from global (time-variable) gravity field. *Journal of Geodynamics*, *39*(3), 223-230.

Dahle, C., Flechtner, F., Gruber, C., König, D., König, R., Michalak, G., & Neumayer, K.-H. (2014). GFZ RL05: An Improved Time-Series of Monthly GRACE Gravity Field Solutions. In F. Flechtner, N. Sneeuw, & W.-D. Schuh (Eds.), *Observation of the System Earth from Space - CHAMP, GRACE, GOCE and future missions: GEOTECHNOLOGIEN Science Report No. 20* (pp. 29–39). Berlin, Heidelberg: Springer Berlin Heidelberg. Retrieved from `https://doi.org/10.1007/978-3-642-32135-1_4` doi: 10.1007/978-3-642-32135-1_4

Daras, I., & Pail, R. (2017). Treatment of temporal aliasing effects in the context of next generation satellite gravimetry missions. *Journal of Geophysical Research: Solid Earth*. Retrieved from `http://dx.doi.org/10.1002/2017JB014250` doi: 10.1002/2017JB014250

Dee, D., Uppala, S., Simmons, A., Berrisford, P., Poli, P., Kobayashi, S., ... others (2011). The ERA-Interim reanalysis: Configuration and performance of the data assimilation system. *Quarterly Journal of the royal meteorological society*, *137*(656), 553–597.

Dobslaw, H., Bergmann-Wolf, I., Dill, R., Forootan, E., Klemann, V., Kusche, J., & Sasgen, I. (2015). The updated ESA Earth System Model for future gravity mission simulation studies. *Journal of Geodesy*, *89*(5), 505–513.

Dobslaw, H., Bergmann-Wolf, I., Dill, R., Poropat, L., & Flechtner, F. (2017a). Product Description Document for AOD1B Release 06. *GFZ Scientic Technical Report*.

Dobslaw, H., Bergmann-Wolf, I., Dill, R., Poropat, L., Thomas, M., Dahle, C., ... Flechtner,

F. (2017b). A new high-resolution model of non-tidal atmosphere and ocean mass variability for de-aliasing of satellite gravity observations: AOD1B RL06. *Geophysical Journal International*, *211*(1), 263–269.

Dobslaw, H., & Thomas, M. (2005). Atmospheric induced oceanic tides from ECMWF forecasts. *Geophysical Research Letters*, *32*(10), 189-191.

Duan, J., Shum, C., Guo, J., & Huang, Z. (2012). Uncovered spurious jumps in the GRACE atmospheric de-aliasing data: potential contamination of GRACE observed mass change. *Geophysical Journal International*, *191*(1), 83–87.

ECMWF. (2015a). IFS documentation-cy41r1. part III: Dynamics and numerical procedures.

ECMWF. (2015b). IFS Documentation-Cy41r1. Part IV: Physical processes. .

Famiglietti, J. S., & Rodell, M. (2013). Water in the balance. *Science*, *340*(6138), 1300–1301.

Flechtner, F., Dobslaw, H., & Fagiolini, E. (2014). AOD1B product description document for product release 05 (Rev. 4.2, May 20, 2014). *Technical Note, GFZ German Research Centre for Geosciences Department*, *1*.

Flechtner, F., Neumayer, K. H., Dahle, C., Dobslaw, H., Fagiolini, E., Raimondo, J. C., & Gntner, A. (2016). What can be expected from the GRACE-FO laser ranging interferometer for Earth science applications? *Surveys in Geophysics*, *37*(2), 453-470.

Forootan, E. (2014). Statistical signal decomposition techniques for analyzing time-variable satellite gravimetry data. *PhD thesis, University of Bonn*. Retrieved from `https://dgk.badw.de/fileadmin/user_upload/Files/DGK/docs/c-763.pdf`

Forootan, E., Didova, O., Kusche, J., & Löcher, A. (2013). Comparisons of atmospheric data and reduction methods for the analysis of satellite gravimetry observations. *Journal of Geophysical Research: Solid Earth*, *118*(5), 2382–2396.

Forootan, E., Didova, O., Schumacher, M., Kusche, J., & Elsaka, B. (2014). Comparisons of atmospheric mass variations derived from ECMWF reanalysis and operational fields, over 2003-2011. *Journal of Geodesy*, *88*(5), 503–514.

Ghobadi-Far, K., Han, S.-C., McCullough, C. M., Wiese, D. N., Yuan, D.-N., Landerer, F. W., ... Watkins, M. M. (2020). GRACE Follow-On Laser Ranging Interferometer Measurements Uniquely Distinguish Short-Wavelength Gravitational Perturbations. *Geophysical Research Letters*, *47*(16). Retrieved from `https://`

agupubs.onlinelibrary.wiley.com/doi/abs/10.1029/2020GL089445 doi: 10.1029/2020GL089445

Gruber, T. (2010). Assessment of a next generation gravity mission for monitoring the variations of earth's gravity field. *Final Report, European Space Agency (ESA) and Astrium GmbH*.

Han, S.-C., Kim, H., Yeo, I.-Y., Yeh, P., Oki, T., Seo, K.-W., ... Luthcke, S. B. (2009). Dynamics of surface water storage in the Amazon inferred from measurements of inter-satellite distance change. *Geophysical Research Letters*, *36*(9).

Hardy, R., Nerem, R., & Wiese, D. (2017). The impact of atmospheric modeling errors on GRACE estimates of mass loss in greenland and antarctica. *Journal of Geophysical Research*, doi:10.1002/2017JB014556.

Hauk, M., & Pail, R. (2018, 07). Treatment of ocean tide aliasing in the context of a next generation gravity field mission. *Geophysical Journal International*, *214*, 345-365. doi: 10.1093/gji/ggy145

Hersbach, H., Bell, B., Berrisford, P., & et al. (2020). The ERA5 global reanalysis. *Quarterly Journal of the Royal Meteorological Society*, *146*(730), 1999-2049. Retrieved from https://rmets.onlinelibrary.wiley.com/doi/abs/10.1002/qj.3803 doi: 10.1002/qj.3803

Kim, J. (2000). Simulation study of a low-low satellite-to-satellite tracking mission. *PhD thesis, The University of Texas at Austin*.

Kornfeld, R. P., Arnold, B. W., Gross, M. A., Dahya, N. T., Klipstein, W. M., Gath, P. F., & Bettadpur, S. (2019). GRACE-FO: The Gravity Recovery and Climate Experiment Follow-On Mission. *Journal of Spacecraft and Rockets*, *56*(3), 931-951. Retrieved from https://doi.org/10.2514/1.A34326 doi: 10.2514/1.A34326

Kusche, J., Klemann, V., & Bosch, W. (2012). Mass distribution and mass transport in the Earth system. *Journal of Geodynamics*, *59*, 1–8.

Lasser, M., Meyer, U., Jggi, A., Mayer-Grr, T., & Flury, J. (2020). Benchmark data for verifying background model implementations in orbit and gravity field determination software. *Advances in Geosciences*, *55*, 1-11.

Liu, H., Lin, P., Yu, Y.-Q., Wang, F., Liu, X., & Zhang, X. (2014, 01). LASG/IAP climate system ocean model version 2: LICOM2. In (p. 15-26). doi: 10.1007/978-3-642-41801-3_3

Loomis, B. D., Rachlin, K. E., Wiese, D. N., Landerer, F. W., & Luthcke, S. B.

(2020). Replacing GRACE/GRACE-FO With Satellite Laser Ranging: Impacts on Antarctic Ice Sheet Mass Change. *Geophysical Research Letters*, *47*(3), e2019GL085488. Retrieved from https://agupubs.onlinelibrary.wiley.com/doi/abs/10.1029/2019GL085488 (e2019GL085488 10.1029/2019GL085488) doi: https://doi.org/10.1029/2019GL085488

Mehrnegar, N., Jones, O., Singer, M. B., Schumacher, M., Jagdhuber, T., Scanlon, B. R., ... Forootan, E. (2021). Exploring groundwater and soil water storage changes across the CONUS at 12.5km resolution by a Bayesian integration of GRACE data into W3RA. *Science of The Total Environment*, *758*, 143579. Retrieved from https://www.sciencedirect.com/science/article/pii/S0048969720371102 doi: https://doi.org/10.1016/j.scitotenv.2020.143579

Pail, R., Chen, Q., Engels, J., Hauk, M., Liu, W., Purkhauser, A., ... van Dam, T. (2018). Additional constellation and scientific analysis of the next generation gravity mission concept (addcon). *Technical report, Technical University of Munich, Issue 3.1, ESA Contract No. 4000118480/16/NL/FF/gp*.

Panet, I., Sylvain, B., Narteau, C., Rmy, D., & Lemoine, J.-M. (2018, 05). Migrating pattern of deformation prior to the Tohoku-Oki earthquake revealed by GRACE data. *Nature Geoscience*, *11*. doi: 10.1038/s41561-018-0099-3

Petit, G., & Luzum, B. (2010, January). IERS Conventions (2010). *IERS Technical Note*.

Ponte, R. M. (1993). Variability in a homogeneous global ocean forced by barometric pressure. *Dynamics of Atmospheres and Oceans*, *18*(3), 209-234. Retrieved from https://www.sciencedirect.com/science/article/pii/0377026593900105 doi: https://doi.org/10.1016/0377-0265(93)90010-5

Poropat, L., Kvas, A., Mayer-Grr, T., & Dobslaw, H. (2019, 10). Mitigating temporal aliasing effects of high-frequency geophysical fluid dynamics in satellite gravimetry. *Geophysical Journal International*, *220*(1), 257-266. Retrieved from https://doi.org/10.1093/gji/ggz439 doi: 10.1093/gji/ggz439

Ramillien, G., Biancale, R., Gratton, S., Vasseur, X., & S, B. (2011). GRACE-derived surface water mass anomalies by energy integral approach: application to continental hydrology. *Journal of Geodesy*, *85*, 313–328, doi:10.1007/s00190-010-0438-7.

Rieser, D., Mayer-Gurr, T., Savcenko, R., Bosch, W., Wunsch, J., Dahle, C., & Flechtner, F. (2012). The ocean tide model EOT11a in spherical harmonics representation . *Technical Note*.

Sasgen, I., Konrad, H., Ivins, E., Van den Broeke, M., Bamber, J., Martinec, Z., & Klemann, V. (2013). Antarctic ice-mass balance 2003 to 2012: regional reanalysis of GRACE satellite gravimetry measurements with improved estimate of glacial-isostatic adjustment based on GPS uplift rates. *The Cryosphere*, *7*, 1499–1512.

Schindelegger, M., & Ray, R. (2014, 12). Surface pressure tide climatologies deduced from a quality-controlled network of barometric observations. *Monthly Weather Review*, *142*, 48724889. doi: 10.1175/MWR-D-14-00217.1

Schumacher, M., Forootan, E., van Dijk AIJM, Müller Schmied, H., Crosbie, R., Kusche, J., & Döll, P. (2018). Improving drought simulations within the Murray-Darling Basin by combined calibration/assimilation of GRACE data into the WaterGAP Global Hydrology Model. *Remote Sensing of Environment*, *204*, 212–228, doi:10.1016/j.rse.2017.10.029.

Sneeuw, N. (1994). Global spherical harmonic analysis by least-squares and numerical quadrature methods in historical perspective. *Geophysical Journal International*, *118*(3), 707-716. Retrieved from `https://onlinelibrary.wiley.com/doi/abs/10.1111/j.1365-246X.1994.tb03995.x` doi: 10.1111/j.1365-246X.1994.tb03995.x

Swenson, S., & Wahr, J. (2002). Estimated effects of the vertical structure of atmospheric mass on the time-variable geoid. *Journal of Geophysical Research: Solid Earth*, *107*(B9). Retrieved from `https://agupubs.onlinelibrary.wiley.com/doi/abs/10.1029/2000JB000024` doi: 10.1029/2000JB000024

Tapley, B., Bettadpur, S., Watkins, M., & Reigber, C. (2004). The gravity recovery and climate experiment: Mission overview and early results. *Geophysical Research Letters*, *31*(9).

Tapley, B., Watkins, M., Flechtner, F., & et al. (2019). Contributions of GRACE to understanding climate change. *Nat. Clim. Chang.*, *9*, 358369. doi: https://doi.org/10.1038/s41558-019-0456-2

Velicogna, I., Mohajerani, Y., A, G., Landerer, F., & et al. (2020). Continuity of Ice Sheet Mass Loss in Greenland and Antarctica From the GRACE and GRACE Follow-On Missions. *Geophysical Research Letters*, *47*(8), e2020GL087291. Retrieved from `https://agupubs.onlinelibrary.wiley.com/doi/abs/10.1029/2020GL087291` doi: 10.1029/2020GL087291

Vielberg, K., Forootan, E., Lück, C., Löcher, A., Kusche, J., & Börger, K. (2018). Comparison of accelerometer data calibration methods used in thermospheric neutral density estimation. *Annales Geophysicae*, *36*(3), 761–779. Retrieved from https://angeo.copernicus.org/articles/36/761/2018/ doi: 10.5194/angeo-36-761-2018

Wahr, J., Molenaar, M., & Bryan, F. (1998). Time variability of the earth's gravity field: Hydrological and oceanic effects and their possible detection using grace. *Journal of Geophysical Research Solid Earth*, *103*(B12).

Wang, H., Xiang, L., Jia, L., Jiang, L., Wang, Z., Bo, H., & Peng, G. (2012). Load Love numbers and Green's functions for elastic Earth models PREM, iasp91, ak135, and modified models with refined crustal structure from Crust 2.0. *Computers and Geosciences*, *49*, 190-199.

Wen, H. Y., Kruizinga, G., Paik, M., Landerer, F., Bertiger, W., Sakumura, C., ... Mccullough, C. (2019). Gravity Recovery and Climate Experiment Follow-On (GRACE-FO) Level-1 Data Product User Handbook. *JPL Publication D-56935 (URS270772)*.

Yang, F. (2021, 2). Ocean mask and atmospheric tide derived from ERA5. *Figshow*. Retrieved from https://figshare.com/articles/dataset/Ocean_mask_and_atmospheric_tide_derived_from_ERA5/14113010 doi: 10.6084/m9.figshare.14113010.v1

Yang, F., Forootan, E., Schumacher, M., Shum, C., & Zhong, M. (2018, 08). Evaluating non-tidal atmospheric products by measuring GRACE K-band range rate residuals. *Geophysical Journal International*, *215*(2), 1132-1147. Retrieved from https://doi.org/10.1093/gji/ggy340 doi: 10.1093/gji/ggy340

Yang, F., Kusche, J., Forootan, E., & Rietbroek, R. (2017). Passiveocean radial basis function approach to improve temporal gravity recovery from grace observations. *Journal of Geophysical Research Solid Earth*, *122*(8).

Yang, F., & Luo, Z. (2021, 01). HUST-ERA5, an hourly global atmospheric de-aliasing product (2002-2020). *National Tibetan Plateau Data Center*. Retrieved from http://dx.doi.org10.11888/Geo.tpdc.271147 doi: 10.11888/Geo.tpdc.271147

Young, D. M., & Gregory, R. T. (1988). *A Survey of Numerical Mathematics.* Dover Publications, Incorporated.

Zingerle, P., Pail, R., Gruber, T., & Oikonomidou, X. (2020). The combined global gravity field model XGM2019e. *Journal of Geodesy*, *94*(7), 66. doi: 10.1007/s00190-020-01398-0